

# High-order accurate entropy stable adaptive moving mesh finite difference schemes for (multi-component) compressible Euler equations with the stiffened equation of state

Shangting Li, Junming Duan\*

*Center for Applied Physics and Technology, HEDPS and LMAM, School of Mathematical Sciences, Peking University, Beijing 100871, P.R. China*

Huazhong Tang\*\*

*Nanchang Hangkong University, Jiangxi Province, Nanchang 330000, P.R. China; Center for Applied Physics and Technology, HEDPS and LMAM, School of Mathematical Sciences, Peking University, Beijing 100871, P.R. China*

---

## Abstract

This paper extends the high-order entropy stable (ES) adaptive moving mesh finite difference schemes developed in [14] to the two- and three-dimensional (multi-component) compressible Euler equations with the stiffened equation of state. The two-point entropy conservative (EC) flux is first constructed in the curvilinear coordinates. The high-order semi-discrete EC schemes are given with the aid of the two-point EC flux and the high-order discretization of the geometric conservation laws, and then the high-order semi-discrete ES schemes satisfying the entropy inequality are derived by adding the high-order dissipation term based on the multi-resolution weighted essentially non-oscillatory (WENO) reconstruction for the scaled entropy variables to the EC schemes. The explicit strong-stability-preserving Runge-Kutta methods are used for the time discretization and the mesh points are adaptively redistributed by iteratively solving the mesh redistribution equations with an appropriately chosen monitor function. Several 2D and 3D numerical tests are conducted on the parallel computer system with the MPI programming to validate the accuracy and the ability to capture effectively the localized structures of the proposed schemes.

*Keywords:* Entropy stability, entropy conservation, mesh redistribution, (multi-component) compressible Euler equations, stiffened equation of state

---

\*Current address: École polytechnique Fédérale de Lausanne, 1015 Lausanne, Switzerland.

\*\*Corresponding author. Fax: +86-10-62751801.

*Email addresses:* shangt1@pku.edu.cn (Shangting Li), duanjm@pku.edu.cn (Junming Duan), hztang@math.pku.edu.cn (Huazhong Tang)

## 1. Introduction

This paper is concerned with the high-order accurate entropy stable (ES) adaptive moving mesh finite difference schemes for the  $d$ -dimensional (multi-component) compressible Euler equations [30]

$$\begin{aligned} \frac{\partial \mathbf{U}}{\partial t} + \sum_{k=1}^d \frac{\partial \mathbf{F}_k(\mathbf{U})}{\partial x_k} &= 0, \\ \mathbf{U} &= (\rho_1, \dots, \rho_N, \rho \mathbf{v}^\top, E)^\top, \\ \mathbf{F}_k &= (\rho_1 v_k, \dots, \rho_N v_k, \rho v_k \mathbf{v}^\top + p \mathbf{e}_k^\top, (E + p)v_k)^\top, \end{aligned} \tag{1.1}$$

where  $d = 2$  or  $3$ ,  $\rho_\ell$  denotes the  $\ell$ th species density,  $\ell = 1, \dots, N$ ,  $\rho = \sum_{\ell=1}^N \rho_\ell$  is the total density,  $\mathbf{v} = (v_1, \dots, v_d)^\top$  denotes the velocity vector,  $\mathbf{e}_k$  is the  $k$ th column of the  $d \times d$  unit matrix, and  $E = \rho e + \rho |\mathbf{v}|^2 / 2$  is the total energy with the specific internal energy  $e$ . Assume that the  $N$  species fluids are in thermal equilibrium and the pressure mixture  $p$  is governed by the stiffened equation of state (EOS) [42]

$$\frac{p + p_\infty}{\Gamma - 1} + p_\infty = \rho e = \sum_{\ell=1}^N \rho_\ell e_\ell, \quad \rho_\ell e_\ell = c_{v,\ell} \rho_\ell T + p_{\infty,\ell},$$

where  $T$  is the temperature,  $p_{\infty,\ell}$  is the pressure constant related to the material, and  $\Gamma := \left( \sum_{\ell=1}^N \Gamma_\ell c_{v,\ell} \rho_\ell \right) / \left( \sum_{\ell=1}^N c_{v,\ell} \rho_\ell \right)$  with the specific heat at constant volume  $c_{v,\ell}$  and the  $\ell$ th species adiabatic index  $\Gamma_\ell$ , see e.g. [30]. If taking  $p_\infty = \sum_{\ell=1}^N p_{\infty,\ell}$ , then the above EOS can be rewritten as follows

$$p = \sum_{\ell=1}^N (\rho_\ell R_\ell T - p_{\infty,\ell}), \tag{1.2}$$

with  $R_\ell = c_{v,\ell} (\Gamma_\ell - 1)$ . The stiffened EOS is often used when considering water under very high pressures (typical applications are underwater nuclear explosions and sonic shock lithotripsy etc.). If  $p_{\infty,\ell} = 0$ ,  $\ell = 1, \dots, N$ , then (1.2) reduces to the ideal gas EOS. The multi-component ( $N$  species) compressible Euler equations (1.1) can also be viewed as the ‘‘one-component’’ compressible Euler equations complemented with  $N - 1$  species mass-conservation equations [23]. In view of this, one may discretize the multi-component ( $N$  species) compressible Euler equations (1.1) wholly, see e.g. [29, 18, 42], or discretize the ‘‘one-component’’ compressible Euler equations and the complemented  $N - 1$  species equations separately, see e.g. [25]. Besides, the level-set methods [12, 37], the volume-of-fluid methods [35, 38], and the BGK-based method [53] were also studied for the multi-component Euler equations. Even if the initial data are sufficiently smooth, the quasi-linear hyperbolic conservation laws such as (1.1) may have discontinuous solutions so that one should consider the weak solutions which are not unique in general and single out the physically relevant solution among all the weak solutions by the entropy condition etc.

**Definition 1.1** (Entropy function). *A scalar function  $\eta(\mathbf{U})$  is called an entropy function for the system (1.1) if there exist associated entropy fluxes  $q_k(\mathbf{U})$  satisfying*

$$q'_k(\mathbf{U}) = \mathbf{V}^\top \mathbf{F}'_k(\mathbf{U}), \quad k = 1, \dots, d,$$

where  $\mathbf{V} = \eta'(\mathbf{U})^\top$  is called the entropy variables and  $(\eta, q_k)$  forms an entropy pair. Further, one can define the entropy potential  $\phi$  and corresponding flux  $\psi_k$  by using the conjugate variables as follows

$$\phi := \mathbf{V}^\top \mathbf{U} - \eta, \quad \psi_k := \mathbf{V}^\top \mathbf{F}_k - q_k.$$

If there exists a strictly convex entropy pair for the hyperbolic conservation laws (1.1),  $\eta''(\mathbf{U}) > 0$ , then the entropy solution should satisfy the following entropy condition

$$\frac{\partial \eta(\mathbf{U})}{\partial t} + \sum_{k=1}^d \frac{\partial q_k(\mathbf{U})}{\partial x_k} \leq 0, \quad (1.3)$$

where the equality holds for the smooth solutions, while the inequality is for the nonsmooth solutions in the sense of distributions.

Integrating (1.3) in space with periodic or zero entropy flux boundary conditions, the total amount of the entropy  $\int \eta(\mathbf{U}(\cdot, t)) d\mathbf{x}$  decreases in time. This is a generalization of the  $L^2$ -energy bound encountered in the linear case [45]. To select the physically relevant solution, it is important to construct the high-order accurate entropy conservative (EC) or ES schemes which satisfy a discrete or semi-discrete version of the entropy condition (1.3). The framework of the second-order EC scheme which satisfies the semi-discrete entropy identity was established in [44, 45], and the higher-order extension was introduced in [33]. It should be noticed that the EC schemes may produce oscillations near the discontinuities so that some numerical dissipative terms need to be added to obtain the ES schemes which suppress possible oscillations [19]. With the help of the summation-by-parts (SBP) operators [9, 21], the ES discontinuous Galerkin (DG) schemes were developed, including the space-time DG method [26], the DG spectral element methods [21, 9] and the DG methods on the unstructured simplex meshes [11]. Recently, the EC or ES schemes were extended to the relativistic hydrodynamic equations [1, 15, 17], the relativistic magnetohydrodynamic equations [14, 16, 52], the multi-component Euler equations [23, 41], and so on.

Adaptive moving mesh methods have been playing an important role in solving partial differential equations due to improving the efficiency and quality of the numerical computations, including the grid redistribution approaches [4, 5, 40, 48, 50], the moving finite element methods [13, 36] and the moving mesh PDEs methods [8, 10, 43]. The readers are referred to the review articles [7, 46] and references therein. This paper focuses on the high-order ES adaptive moving mesh finite

difference schemes for the (multi-component) compressible Euler equations ( $N = 1, 2$ ) with the stiffened EOS. The two-point EC fluxes for the (multi-component) compressible Euler equations with the stiffened EOS are explicitly derived in curvilinear coordinates, and then are combined with the high-order discrete geometric conservation laws to give the high-order EC fluxes. The high-order ES fluxes in curvilinear coordinates are obtained by adding appropriate dissipation terms into the high-order EC fluxes, which are built on the jump of the high-order accurate multi-resolution WENO reconstruction values of the scaled entropy variables. The mesh adaptation is implemented by iteratively solving the Euler-Lagrange equations of the mesh adaptation functional in the computational domain with appropriate monitor function. Compared to the single-component case, the monitor function needs to contain more information on the solutions of the multi-component compressible Euler equations to produce high-quality mesh. The semi-discrete schemes are equipped with the third-order accurate explicit strong-stability preserving (SSP) Runge-Kutta (RK) schemes to obtain the fully-discrete schemes.

This paper is organized as follows. Section 2 introduces the form of the system (1.1) in the curvilinear coordinates and corresponding entropy conditions. Section 3 gives a sufficient condition for the EC fluxes, two-point EC fluxes, the high-order discrete geometric conservation laws, and the high-order EC and ES schemes for the (multi-component) compressible Euler equations with the stiffened EOS in curvilinear coordinates. Adaptive moving mesh strategy is presented in Section 4. Several 2D and 3D numerical results are presented in Section 5 to validate the effectiveness and performance of our schemes on the parallel computer system with the MPI communication. Section 6 gives some conclusions.

## 2. Entropy conditions in curvilinear coordinates

This section introduces the entropy conditions in curvilinear coordinates similar to that in [14]. The adaptive moving meshes in the physical domain  $\Omega_p$  with coordinates  $\mathbf{x} = (x_1, \dots, x_d)$  can be generated as the images of a reference mesh in the computational domain  $\Omega_c$  with coordinates  $\boldsymbol{\xi} = (\xi_1, \dots, \xi_d)$  by a time dependent, differentiable, one-to-one coordinate mapping  $\mathbf{x} = \mathbf{x}(\boldsymbol{\xi}, t)$ , which can be expressed as

$$t = \tau, \quad \mathbf{x} = \mathbf{x}(\boldsymbol{\xi}, \tau), \quad \boldsymbol{\xi} = (\xi_1, \dots, \xi_d) \in \Omega_c, \quad (2.1)$$

under which the system (1.1) can be transformed as the following conservative form

$$\frac{\partial(JU)}{\partial\tau} + \sum_{k=1}^d \frac{\partial}{\partial\xi_k} \left[ \left( J \frac{\partial\xi_k}{\partial t} U \right) + \sum_{j=1}^d \left( J \frac{\partial\xi_k}{\partial x_j} F_j \right) \right] = 0, \quad (2.2)$$

where  $J = \det \left( \frac{\partial(t, \mathbf{x})}{\partial(\tau, \boldsymbol{\xi})} \right)$ . For (2.1), one has the following geometric conservation laws (GCLs)

$$\begin{aligned} \text{VCL: } & \frac{\partial J}{\partial \tau} + \sum_{k=1}^d \frac{\partial}{\partial \xi_k} \left( J \frac{\partial \xi_k}{\partial t} \right) = 0, \\ \text{SCLs: } & \sum_{k=1}^d \frac{\partial}{\partial \xi_k} \left( J \frac{\partial \xi_k}{\partial x_j} \right) = 0, \quad j = 1, \dots, d, \end{aligned} \quad (2.3)$$

where the volume conservation law (VCL) implies that the volumetric increment of a moving cell is equal to the sum of the changes along the surfaces that enclose the cell, while the surface conservation laws (SCLs) indicate that the cell volume should be closed by its surfaces [54].

Utilizing (2.2) and the GCLs (2.3) can derive the entropy condition in curvilinear coordinates

$$\frac{\partial(J\eta)}{\partial \tau} + \sum_{k=1}^d \frac{\partial}{\partial \xi_k} \left[ \left( J \frac{\partial \xi_k}{\partial t} \eta \right) + \sum_{j=1}^d \left( J \frac{\partial \xi_k}{\partial x_j} q_j \right) \right] \leq 0,$$

where the equality holds for the smooth solutions of (1.1), and the inequality is in the sense of distributions for the nonsmooth solutions.

### 3. Numerical schemes

This section only presents the 3D moving mesh EC and ES schemes for the system (2.2) on the structured hexahedral mesh following [14], because the 2D schemes can be considered as the degenerative case, see the appendices in [14] for more details.

Let us choose  $\Omega_c$  as a cuboid  $[a_1, b_1] \times [a_2, b_2] \times [a_3, b_3]$  and divide it into a fixed orthogonal uniform mesh  $\{(\xi_{1,i_1}, \xi_{2,i_2}, \xi_{3,i_3}): a_k = \xi_{k,1} < \dots < \xi_{k,i_k} < \dots < \xi_{k,N_k} = b_k, k = 1, 2, 3\}$  with the constant mesh size  $\Delta \xi_k = \xi_{k,i_k+1} - \xi_{k,i_k}$ . For the sake of brevity, the index  $\mathbf{i} = (i_1, i_2, i_3)$  denotes the point  $(\xi_{1,i_1}, \xi_{2,i_2}, \xi_{3,i_3})$  and the notation  $\{\mathbf{i}, k, m\}$  means that the index  $\mathbf{i}$  increases  $m$  along  $i_k$ -direction, e.g.  $\{\mathbf{i}, 1, \frac{1}{2}\}$  is  $(i_1 + \frac{1}{2}, i_2, i_3)$ .

Consider the following semi-discrete conservative  $2w$ -order ( $w \geq 1$ ) finite difference schemes for (2.2) and the first equation in (2.3)

$$\frac{d}{dt} (JU)_{\mathbf{i}} = - \sum_{k=1}^3 \frac{1}{\Delta \xi_k} \left( \left( \widehat{\mathbf{F}}_k \right)_{\mathbf{i}, k, +\frac{1}{2}}^{2wth} - \left( \widehat{\mathbf{F}}_k \right)_{\mathbf{i}, k, -\frac{1}{2}}^{2wth} \right), \quad (3.1)$$

$$\frac{d}{dt} J_{\mathbf{i}} = - \sum_{k=1}^3 \frac{1}{\Delta \xi_k} \left( \left( \widehat{J \frac{\partial \xi_k}{\partial t}} \right)_{\mathbf{i}, k, +\frac{1}{2}}^{2wth} - \left( \widehat{J \frac{\partial \xi_k}{\partial t}} \right)_{\mathbf{i}, k, -\frac{1}{2}}^{2wth} \right), \quad (3.2)$$

where  $J_{\mathbf{i}}(t)$  and  $(JU)_{\mathbf{i}}(t)$  approximate the point values of  $J(t, \boldsymbol{\xi})$  and  $(JU)(t, \boldsymbol{\xi})$  at  $\mathbf{i}$ , respectively,  $\left( \widehat{\mathbf{F}}_k \right)_{\mathbf{i}, k, \pm \frac{1}{2}}^{2wth}(t)$  is the numerical flux approximating the continuous flux  $\left( J \frac{\partial \xi_k}{\partial t} \mathbf{U} + \sum_{j=1}^3 J \frac{\partial \xi_k}{\partial x_j} \mathbf{F}_j \right)(t, \boldsymbol{\xi})$

at  $\{\mathbf{i}, k, \pm\frac{1}{2}\}$ ,  $k = 1, 2, 3$ , and  $\left(\widehat{J\frac{\partial\xi_k}{\partial t}}\right)_{\mathbf{i},k,\pm\frac{1}{2}}^{2wth}$  is the flux approximating the metric  $J\frac{\partial\xi_k}{\partial t}$  at  $\{\mathbf{i}, k, \pm\frac{1}{2}\}$ , which is used to update the metric Jacobian  $J_{\mathbf{i}}$ , see (3.7) in Section 3.1. Corresponding discrete version of the SCLs in (2.3) will be of the form

$$\sum_{k=1}^3 \frac{1}{\Delta\xi_k} \left( \left(\widehat{J\frac{\partial\xi_k}{\partial x_j}}\right)_{\mathbf{i},k,+\frac{1}{2}}^{2wth} - \left(\widehat{J\frac{\partial\xi_k}{\partial x_j}}\right)_{\mathbf{i},k,-\frac{1}{2}}^{2wth} \right) = 0, \quad j = 1, 2, 3. \quad (3.3)$$

**Definition 3.1.** *The semi-discrete scheme (3.1)-(3.2) or its flux is EC, if its solution satisfies the semi-discrete entropy identity*

$$\frac{d}{dt} J_{\mathbf{i}} \eta(\mathbf{U}_{\mathbf{i}}(t)) + \sum_{k=1}^3 \frac{1}{\Delta\xi_k} \left( (\widehat{q}_k)_{\mathbf{i},k,+\frac{1}{2}}^{2wth}(t) - (\widehat{q}_k)_{\mathbf{i},k,-\frac{1}{2}}^{2wth}(t) \right) = 0, \quad (3.4)$$

where the numerical entropy flux  $(\widehat{q}_k)_{\mathbf{i},k,\pm\frac{1}{2}}^{2wth}$  is consistent with the entropy flux  $J\frac{\partial\xi_k}{\partial t}\eta + \sum_{j=1}^3 J\frac{\partial\xi_k}{\partial x_j}q_j$ .

### 3.1. A sufficient condition for the EC fluxes

Similar to the special relativistic (magneto)hydrodynamics in [14], one can deduce the following sufficient condition for the two-point EC fluxes of (3.1).

**Proposition 3.1.** *If a two-point flux  $\widehat{\mathbf{F}}_k \left( \mathbf{U}_l, \mathbf{U}_r, \left( J\frac{\partial\xi_k}{\partial\zeta} \right)_l, \left( J\frac{\partial\xi_k}{\partial\zeta} \right)_r \right)$ ,  $\zeta = t, x_1, x_2, x_3$ , being consistent with  $J\frac{\partial\xi_k}{\partial t}\mathbf{U} + \sum_{j=1}^3 J\frac{\partial\xi_k}{\partial x_j}\mathbf{F}_j$ , satisfies*

$$\begin{aligned} (\mathbf{V}(\mathbf{U}_r) - \mathbf{V}(\mathbf{U}_l))^T \widehat{\mathbf{F}}_k &= \frac{1}{2} \left( \left( J\frac{\partial\xi_k}{\partial t} \right)_l + \left( J\frac{\partial\xi_k}{\partial t} \right)_r \right) (\phi(\mathbf{U}_r) - \phi(\mathbf{U}_l)) \\ &+ \sum_{j=1}^3 \frac{1}{2} \left( \left( J\frac{\partial\xi_k}{\partial x_j} \right)_l + \left( J\frac{\partial\xi_k}{\partial x_j} \right)_r \right) (\psi_j(\mathbf{U}_r) - \psi_j(\mathbf{U}_l)), \end{aligned} \quad (3.5)$$

then the scheme (3.1) is EC, where the subscripts  $l$  and  $r$  represent two states, denoted respectively by the left and right states.

If the two-point EC flux  $\widehat{\mathbf{F}}_k \left( \mathbf{U}_l, \mathbf{U}_r, \left( J\frac{\partial\xi_k}{\partial\zeta} \right)_l, \left( J\frac{\partial\xi_k}{\partial\zeta} \right)_r \right)$  satisfying (3.5) is symmetric,  $\zeta = t, x_1, x_2, x_3$ , then one can further derive the semi-discrete  $2wth$ -order EC schemes (3.1)-(3.2) with the following  $2wth$ -order EC fluxes

$$\left(\widehat{\mathbf{F}}_k\right)_{\mathbf{i},k,+\frac{1}{2}}^{2wth} = \sum_{m=1}^w \alpha_{w,m} \sum_{s=0}^{m-1} \widehat{\mathbf{F}}_k \left( \mathbf{U}_{\mathbf{i},k,-s}, \mathbf{U}_{\mathbf{i},k,-s+m}, \left( J\frac{\partial\xi_k}{\partial\zeta} \right)_{\mathbf{i},k,-s}, \left( J\frac{\partial\xi_k}{\partial\zeta} \right)_{\mathbf{i},k,-s+m} \right), \quad (3.6)$$

$$\left(\widehat{J\frac{\partial\xi_k}{\partial\zeta}}\right)_{\mathbf{i},k,+\frac{1}{2}}^{2wth} = \sum_{m=1}^w \alpha_{w,m} \sum_{s=0}^{m-1} \frac{1}{2} \left( \left( J\frac{\partial\xi_k}{\partial\zeta} \right)_{\mathbf{i},k,-s} + \left( J\frac{\partial\xi_k}{\partial\zeta} \right)_{\mathbf{i},k,-s+m} \right), \quad (3.7)$$

where the constants  $\{\alpha_{w,m}\}$  satisfy the conditions [33]

$$\sum_{m=1}^w m\alpha_{w,m} = 1, \quad \sum_{m=1}^w m^{2s-1}\alpha_{w,m} = 0, \quad s = 2, \dots, w.$$

In this case, corresponding numerical entropy fluxes can be chosen as follows

$$\begin{aligned} (\widehat{q}_k)_{i,k,+\frac{1}{2}}^{2wth} &= \sum_{m=1}^w \alpha_{w,m} \sum_{s=0}^{m-1} \widehat{q}_k \left( \mathbf{U}_{i,k,-s}, \mathbf{U}_{i,k,-s+m}, \left( J \frac{\partial \xi_k}{\partial \zeta} \right)_{i,k,-s}, \left( J \frac{\partial \xi_k}{\partial \zeta} \right)_{i,k,-s+m} \right), \\ \widehat{q}_k \left( \mathbf{U}_l, \mathbf{U}_r, \left( J \frac{\partial \xi_k}{\partial \zeta} \right)_l, \left( J \frac{\partial \xi_k}{\partial \zeta} \right)_r \right) &= \frac{1}{2} (\mathbf{V}(\mathbf{U}_l) + \mathbf{V}(\mathbf{U}_r))^T \widehat{\mathbf{F}}_k \left( \mathbf{U}_l, \mathbf{U}_r, \left( J \frac{\partial \xi_k}{\partial \zeta} \right)_l, \left( J \frac{\partial \xi_k}{\partial \zeta} \right)_r \right) \\ &\quad - \frac{1}{4} \left( \left( J \frac{\partial \xi_k}{\partial t} \right)_l + \left( J \frac{\partial \xi_k}{\partial t} \right)_r \right) (\phi(\mathbf{U}_l) + \phi(\mathbf{U}_r)) \\ &\quad - \sum_{j=1}^3 \frac{1}{4} \left( \left( J \frac{\partial \xi_k}{\partial x_j} \right)_l + \left( J \frac{\partial \xi_k}{\partial x_j} \right)_r \right) (\psi_j(\mathbf{U}_l) + \psi_j(\mathbf{U}_r)). \end{aligned}$$

### 3.2. Discrete GCLs

This section gives the discrete GCLs, which are essential in the proof of the EC or ES property of the schemes. Failing to satisfy discrete GCLs may lead to a misrepresentation of the convective velocities and extra sources or sinks in the physically conservative media [54].

To achieve the discrete SCLs, following [14], the  $2wth$ -order accurate discretizations for  $J \frac{\partial \xi_k}{\partial x_j}$ ,  $k, j = 1, 2, 3$ , can be constructed. For example, when  $j = 1$ , one has

$$\begin{aligned} \left( J \frac{\partial \xi_1}{\partial x_1} \right)_i &= \left( \frac{\partial x_2}{\partial \xi_2} \frac{\partial x_3}{\partial \xi_3} - \frac{\partial x_2}{\partial \xi_3} \frac{\partial x_3}{\partial \xi_2} \right)_i = \frac{1}{\Delta \xi_2 \Delta \xi_3} (\delta_3 [\delta_2 [x_2] x_3] - \delta_2 [\delta_3 [x_2] x_3]), \\ \left( J \frac{\partial \xi_2}{\partial x_1} \right)_i &= \left( \frac{\partial x_2}{\partial \xi_3} \frac{\partial x_3}{\partial \xi_1} - \frac{\partial x_2}{\partial \xi_1} \frac{\partial x_3}{\partial \xi_3} \right)_i = \frac{1}{\Delta \xi_3 \Delta \xi_1} (\delta_1 [\delta_3 [x_2] x_3] - \delta_3 [\delta_1 [x_2] x_3]), \\ \left( J \frac{\partial \xi_3}{\partial x_1} \right)_i &= \left( \frac{\partial x_2}{\partial \xi_1} \frac{\partial x_3}{\partial \xi_2} - \frac{\partial x_2}{\partial \xi_2} \frac{\partial x_3}{\partial \xi_1} \right)_i = \frac{1}{\Delta \xi_1 \Delta \xi_2} (\delta_2 [\delta_1 [x_2] x_3] - \delta_1 [\delta_2 [x_2] x_3]), \end{aligned} \quad (3.9)$$

with the  $2wth$ -order central difference operator in the  $\xi_k$ -direction

$$\delta_k[a_i] = \frac{1}{2} \sum_{m=1}^w \alpha_{w,m} (a_{i,k,+m} - a_{i,k,-m}).$$

Combining (3.9) with the  $2wth$ -order discretizations of the fluxes in (3.7) easily gets the discrete SCLs (3.3).

Regarding the discrete VCL, for the transformation (2.1), one has

$$J \frac{\partial \xi_k}{\partial t} = - \sum_{j=1}^3 \frac{\partial x_j}{\partial t} \left( J \frac{\partial \xi_k}{\partial x_j} \right), \quad k = 1, 2, 3,$$

which can be approximated efficiently and easily by

$$\left( J \frac{\partial \xi_k}{\partial t} \right)_i = - \sum_{j=1}^3 (\dot{x}_j)_i \left( J \frac{\partial \xi_k}{\partial x_j} \right)_i, \quad (3.10)$$

where  $\left(J \frac{\partial \xi_k}{\partial x_j}\right)_i$  is given by (3.9), and  $(\dot{x}_j)_i$ ,  $j = 1, 2, 3$ , are the mesh velocities at  $\mathbf{i}$  and will be determined in Section 4. Combining (3.10) with the fluxes (3.7) can yield the semi-discrete VCL (3.2).

**Remark 3.1.** It is known that violating the free-stream condition may cause large errors and even lead to numerical instabilities for the high-order schemes [47]. It is proved [14] that the free-stream condition is satisfied by our high-order accurate fully-discrete adaptive moving mesh finite difference schemes derived by integrating (3.1)-(3.2) with the third-order accurate explicit SSP RK schemes [22].

### 3.3. Two-point EC flux

This subsection focuses on the construction of a two-point EC flux satisfying (3.5). One can verify that the following flux, similar to that in [17], meets the requirement

$$\begin{aligned} \widehat{\mathbf{F}}_k \left( \mathbf{U}_l, \mathbf{U}_r, \left( J \frac{\partial \xi_k}{\partial \zeta} \right)_l, \left( J \frac{\partial \xi_k}{\partial \zeta} \right)_r \right) &= \frac{1}{2} \left( \left( J \frac{\partial \xi_k}{\partial t} \right)_l + \left( J \frac{\partial \xi_k}{\partial t} \right)_r \right) \widetilde{\mathbf{U}} \\ &+ \sum_{j=1}^3 \frac{1}{2} \left( \left( J \frac{\partial \xi_k}{\partial x_j} \right)_l + \left( J \frac{\partial \xi_k}{\partial x_j} \right)_r \right) \widetilde{\mathbf{F}}_j, \end{aligned} \quad (3.11)$$

where  $\widetilde{\mathbf{U}}$  and  $\widetilde{\mathbf{F}}_j$  satisfy the following conditions, respectively,

$$(\mathbf{V}_r - \mathbf{V}_l)^T \widetilde{\mathbf{U}} = \phi_r - \phi_l, \quad (\mathbf{V}_r - \mathbf{V}_l)^T \widetilde{\mathbf{F}}_j = (\psi_j)_r - (\psi_j)_l. \quad (3.12)$$

In the following, we will give the explicit expressions of the symmetric two-point EC fluxes for the single- and two-component compressible Euler equations ( $N = 1, 2$ ) with the stiffened EOS, separately.

#### 3.3.1. Single-component compressible Euler equations ( $N = 1$ )

This subsection begins to construct the symmetric two-point EC flux for the single-component compressible Euler equations ( $N = 1$ ).

Assume that the numerical solutions satisfy  $\rho_1, T > 0$ , and define the thermodynamic entropy as  $S_1 = c_{v,1} \ln T - R_1 \ln \rho_1$ , see [32]. It is easy to prove that the smooth solutions of (1.1) with  $N = 1$  satisfy

$$\frac{\partial(\rho_1 S_1)}{\partial t} + \sum_{k=1}^3 \frac{\partial(\rho_1 v_k S_1)}{\partial x_k} = 0.$$

If define

$$\eta(\mathbf{U}) = -\rho_1 S_1, \quad q_k(\mathbf{U}) = \eta v_k, \quad (3.13)$$



and

$$\mathbf{V} = \eta'(\mathbf{U})^\top = \left( -S_1 - \frac{|\mathbf{v}|^2}{2T} + c_{v,1}\Gamma_1, \frac{\mathbf{v}^\top}{T}, -\frac{1}{T} \right)^\top,$$

then one can verify that  $\partial\mathbf{U}/\partial\mathbf{V}$  is symmetric positive definite, and the matrix  $\frac{\partial\mathbf{F}_k}{\partial\mathbf{U}} \frac{\partial\mathbf{U}}{\partial\mathbf{V}}$  is symmetric, so that (1.1) can be symmetrized with the change of variables  $\mathbf{U} \rightarrow \mathbf{V}$ , and  $(\eta, q_k)$  forms a convex entropy pair of (1.1) with  $N = 1$ . In this case, the entropy potential  $\phi$  and entropy potential flux  $\psi_k$  are explicitly given by

$$\phi = R_1\rho_1 - \frac{p_{\infty,1}}{T}, \quad \psi_k = \phi v_k, \quad k = 1, 2, 3. \quad (3.14)$$

If choosing the parameter vector as

$$\mathbf{z} = (z_1, z_2, z_3, z_4, z_5)^\top = (\rho_1, \mathbf{v}^\top, 1/T)^\top,$$

and using the identity  $\llbracket ab \rrbracket = \{\{a\}\}\llbracket b \rrbracket + \{\{b\}\}\llbracket a \rrbracket$ , where  $\llbracket a \rrbracket$  and  $\{\{a\}\}$  are the jump and mean of  $a$ , respectively, then the jumps of  $\mathbf{V}$ ,  $\phi$ , and  $\psi_1$  can be rewritten as the following linear combinations of the jumps of  $\mathbf{z}$

$$\left\{ \begin{array}{l} \llbracket \mathbf{V}_1 \rrbracket = c_{v,1} \frac{\llbracket z_5 \rrbracket}{\{\{z_5\}\}^{\ln}} + R_1 \frac{\llbracket z_1 \rrbracket}{\{\{z_1\}\}^{\ln}} - \{\{z_5\}\} \sum_{m=2}^4 \{\{z_m\}\} \llbracket z_m \rrbracket - \frac{1}{2} \sum_{m=2}^4 \{\{z_m^2\}\} \llbracket z_5 \rrbracket, \\ \llbracket \mathbf{V}_m \rrbracket = \{\{z_m\}\} \llbracket z_5 \rrbracket + \{\{z_5\}\} \llbracket z_m \rrbracket, \quad m = 2, 3, 4, \\ \llbracket \mathbf{V}_5 \rrbracket = -\llbracket z_5 \rrbracket, \\ \llbracket \phi \rrbracket = R_1 \llbracket z_1 \rrbracket - p_{\infty,1} \llbracket z_5 \rrbracket, \\ \llbracket \psi_1 \rrbracket = (R_1 \llbracket z_1 \rrbracket - p_{\infty,1} \llbracket z_5 \rrbracket) \{\{z_2\}\} + (R_1 \{\{z_1\}\} - p_{\infty,1} \{\{z_5\}\}) \llbracket z_2 \rrbracket, \end{array} \right. \quad (3.15)$$

where  $\{\{a\}\}^{\ln} := \llbracket a \rrbracket / \llbracket \ln a \rrbracket$ ,  $a > 0$  is the logarithmic mean, see [27]. If substituting (3.15) into (3.12) and equating the coefficients of the same jump terms on each side of the identity (3.12), then

$$\left\{ \begin{array}{l} \frac{R_1}{\{\{z_1\}\}^{\ln}} \tilde{\mathbf{U}}_1 = R_1, \\ -\{\{z_m\}\} \{\{z_5\}\} \tilde{\mathbf{U}}_1 + \{\{z_5\}\} \tilde{\mathbf{U}}_m = 0, \quad m = 2, 3, 4, \\ \frac{c_{v,1}}{\{\{z_5\}\}^{\ln}} \tilde{\mathbf{U}}_1 - \frac{1}{2} \sum_{m=2}^4 \{\{z_m^2\}\} \tilde{\mathbf{U}}_1 + \sum_{m=2}^4 \{\{z_m\}\} \tilde{\mathbf{U}}_m - \tilde{\mathbf{U}}_5 = -p_{\infty,1}, \end{array} \right.$$

and

$$\left\{ \begin{array}{l} \frac{R_1}{\{\{z_1\}\}^{\ln}} \tilde{\mathbf{F}}_{1,1} = R_1 \{\{z_2\}\}, \\ -\{\{z_2\}\} \{\{z_5\}\} \tilde{\mathbf{F}}_{1,1} + \{\{z_5\}\} \tilde{\mathbf{F}}_{1,2} = R_1 \{\{z_1\}\} - p_{\infty,1} \{\{z_5\}\}, \\ -\{\{z_m\}\} \{\{z_5\}\} \tilde{\mathbf{F}}_{1,1} + \{\{z_5\}\} \tilde{\mathbf{F}}_{1,m} = 0, \quad m = 3, 4, \\ \frac{c_{v,1}}{\{\{z_5\}\}^{\ln}} \tilde{\mathbf{F}}_{1,1} - \frac{1}{2} \sum_{m=2}^4 \{\{z_m^2\}\} \tilde{\mathbf{F}}_{1,1} + \sum_{m=2}^4 \{\{z_m\}\} \tilde{\mathbf{F}}_{1,m} - \tilde{\mathbf{F}}_{1,5} = -\{\{z_2\}\} p_{\infty,1}, \end{array} \right.$$

where  $\tilde{\mathbf{U}}_m$  and  $\tilde{\mathbf{F}}_{1,m}$  denote the  $m$ th component of  $\tilde{\mathbf{U}}$  and  $\tilde{\mathbf{F}}_1$  with  $m = 1, \dots, 5$ , respectively. Solving the above two systems of the linear equations yields the expressions of  $\tilde{\mathbf{U}}$  and  $\tilde{\mathbf{F}}_1$  as follows

$$\tilde{\mathbf{U}} = \begin{pmatrix} \{z_1\}^{\ln} \\ \{z_2\} \{z_1\}^{\ln} \\ \{z_3\} \{z_1\}^{\ln} \\ \{z_4\} \{z_1\}^{\ln} \\ \left( \frac{c_{v,1}}{\{z_5\}^{\ln}} - \frac{1}{2} \sum_{m=2}^4 \{z_m^2\} \right) \{z_1\}^{\ln} + \{z_1\}^{\ln} \sum_{m=2}^4 \{z_m\}^2 + p_{\infty,1} \end{pmatrix},$$

$$\tilde{\mathbf{F}}_1 = \begin{pmatrix} \{z_1\}^{\ln} \{z_2\}, \\ \{z_2\} \tilde{\mathbf{F}}_{1,1} + \frac{1}{\{z_5\}} R_1 \{z_1\} - p_{\infty,1} \\ \{z_3\} \tilde{\mathbf{F}}_{1,1} \\ \{z_4\} \tilde{\mathbf{F}}_{1,1} \\ \left( \frac{c_{v,1}}{\{z_5\}^{\ln}} - \frac{1}{2} \sum_{m=2}^4 \{z_m^2\} \right) \tilde{\mathbf{F}}_{1,1} + \sum_{m=2}^4 \left( \{z_m\} \tilde{\mathbf{F}}_{1,m} \right) + p_{\infty,1} \{z_2\} \end{pmatrix}.$$

For  $k = 2, 3$ ,  $\tilde{\mathbf{F}}_k$  may be similarly gotten.

### 3.3.2. Two-component compressible Euler equations ( $N = 2$ )

Similarly, the smooth solutions of the two-component compressible Euler equations (1.1) with the stiffened EOS satisfy

$$\frac{\partial(\rho S)}{\partial t} + \sum_{k=1}^3 \frac{\partial(\rho v_k S)}{\partial x_k} = 0,$$

with the entropy of the mixture

$$\rho S := \sum_{\ell=1}^2 \rho_{\ell} S_{\ell}, \quad S_{\ell} := c_{v,\ell} \ln(T) - R_{\ell} \ln(\rho_{\ell}),$$

where  $S_{\ell}$  is the thermodynamic entropy of species  $\ell$ . With the help of the thermodynamic entropy, the mathematical entropy pair of (1.1) may be defined by

$$\eta(\mathbf{U}) = -\rho S, \quad q_k(\mathbf{U}) = \eta v_k, \quad k = 1, 2, 3. \quad (3.16)$$

Because for  $\rho_1 > 0, \rho_2 > 0, T > 0$ ,  $\frac{\partial \mathbf{U}}{\partial \mathbf{V}}$  is symmetric positive definite, and  $\frac{\partial \mathbf{F}_k}{\partial \mathbf{U}} \frac{\partial \mathbf{U}}{\partial \mathbf{V}}$  is symmetric, so that the equations (1.1) can be symmetrized with  $\eta(\mathbf{U}), q_k(\mathbf{U})$ . In this case, the entropy potential  $\phi$  and the entropy potential flux  $\psi_k$  can be explicitly given by

$$\phi = \sum_{\ell=1}^2 \left( R_{\ell} \rho_{\ell} - \frac{p_{\infty,\ell}}{T} \right), \quad \psi_k = \phi v_k, \quad (3.17)$$

with the entropy variables  $\mathbf{V} = \left( -S_1 - \frac{|\mathbf{v}|^2}{2T} + c_{v,1}\Gamma_1, -S_2 - \frac{|\mathbf{v}|^2}{2T} + c_{v,2}\Gamma_2, \frac{\mathbf{v}^\top}{T}, -\frac{1}{T} \right)^\top$ .

If choosing the parameter vector  $\mathbf{z} = (z_1, z_2, z_3, z_4, z_5, z_6)^\top = (\rho_1, \rho_2, \mathbf{v}^\top, 1/T)^\top$ , then the jumps of the entropy variables  $\mathbf{V}$ , the entropy potential  $\phi$  and the entropy potential flux  $\psi_1$  can be rewritten as

$$\left\{ \begin{array}{l} \llbracket \mathbf{V}_1 \rrbracket = c_{v,1} \frac{\llbracket z_6 \rrbracket}{\{\{z_6\}\}^{\ln}} + R_1 \frac{\llbracket z_1 \rrbracket}{\{\{z_1\}\}^{\ln}} - \{\{z_6\}\} \sum_{m=3}^5 \{\{z_m\}\} \llbracket z_m \rrbracket - \frac{1}{2} \sum_{m=3}^5 \{\{z_m^2\}\} \llbracket z_6 \rrbracket, \\ \llbracket \mathbf{V}_2 \rrbracket = c_{v,2} \frac{\llbracket z_6 \rrbracket}{\{\{z_6\}\}^{\ln}} + R_2 \frac{\llbracket z_2 \rrbracket}{\{\{z_2\}\}^{\ln}} - \{\{z_6\}\} \sum_{m=3}^5 \{\{z_m\}\} \llbracket z_m \rrbracket - \frac{1}{2} \sum_{m=3}^5 \{\{z_m^2\}\} \llbracket z_6 \rrbracket, \\ \llbracket \mathbf{V}_m \rrbracket = \{\{z_m\}\} \llbracket z_6 \rrbracket + \{\{z_6\}\} \llbracket z_m \rrbracket, \quad m = 3, 4, 5, \\ \llbracket \mathbf{V}_6 \rrbracket = -\llbracket z_6 \rrbracket, \\ \llbracket \phi \rrbracket = \sum_{\ell=1}^2 (R_\ell \llbracket z_\ell \rrbracket - p_{\infty,\ell} \llbracket z_6 \rrbracket), \\ \llbracket \psi_1 \rrbracket = \sum_{\ell=1}^2 (R_\ell \llbracket z_\ell \rrbracket - p_{\infty,\ell} \llbracket z_6 \rrbracket) \{\{z_3\}\} + \sum_{\ell=1}^2 (R_\ell \{\{z_\ell\}\} - p_{\infty,\ell} \{\{z_6\}\}) \llbracket z_3 \rrbracket. \end{array} \right. \quad (3.18)$$

Substituting it into (3.12) gives

$$\left\{ \begin{array}{l} \frac{R_1}{\{\{z_1\}\}^{\ln}} \tilde{\mathbf{U}}_1 = R_1, \\ \frac{R_2}{\{\{z_2\}\}^{\ln}} \tilde{\mathbf{U}}_2 = R_2, \\ -\{\{z_m\}\} \{\{z_6\}\} \sum_{\ell=1}^2 \tilde{\mathbf{U}}_\ell + \{\{z_6\}\} \tilde{\mathbf{U}}_m = 0, \quad m = 3, 4, 5, \\ \sum_{\ell=1}^2 \left( \frac{c_{v,\ell}}{\{\{z_6\}\}^{\ln}} \tilde{\mathbf{U}}_\ell \right) - \frac{1}{2} \sum_{m=3}^5 \{\{z_m^2\}\} \sum_{\ell=1}^2 \tilde{\mathbf{U}}_\ell + \sum_{m=3}^5 \{\{z_m\}\} \tilde{\mathbf{U}}_m - \tilde{\mathbf{U}}_6 = -\sum_{\ell=1}^2 p_{\infty,\ell}, \end{array} \right.$$

and

$$\left\{ \begin{array}{l} \frac{R_1}{\{\{z_1\}\}^{\ln}} \tilde{\mathbf{F}}_{1,1} = R_1 \{\{z_3\}\}, \\ \frac{R_2}{\{\{z_2\}\}^{\ln}} \tilde{\mathbf{F}}_{1,2} = R_2 \{\{z_3\}\}, \\ -\{\{z_3\}\} \{\{z_6\}\} \sum_{\ell=1}^2 \tilde{\mathbf{F}}_{1,\ell} + \{\{z_6\}\} \tilde{\mathbf{F}}_{1,3} = \sum_{\ell=1}^2 (R_\ell \{\{z_\ell\}\} - p_{\infty,\ell} \{\{z_6\}\}), \\ -\{\{z_m\}\} \{\{z_6\}\} \sum_{\ell=1}^2 \tilde{\mathbf{F}}_{1,\ell} + \{\{z_6\}\} \tilde{\mathbf{F}}_{1,m} = 0, \quad m = 4, 5, \\ \sum_{\ell=1}^2 \left( \frac{c_{v,\ell}}{\{\{z_6\}\}^{\ln}} \tilde{\mathbf{F}}_{1,\ell} \right) - \frac{1}{2} \sum_{m=3}^5 \{\{z_m^2\}\} \sum_{\ell=1}^2 \tilde{\mathbf{F}}_{1,\ell} + \sum_{m=3}^5 \{\{z_m\}\} \tilde{\mathbf{F}}_{1,m} - \tilde{\mathbf{F}}_{1,6} = -\{\{z_3\}\} \sum_{\ell=1}^2 p_{\infty,\ell}, \end{array} \right.$$

where  $\tilde{\mathbf{F}}_{1,m}$  and  $\tilde{\mathbf{U}}_m$  denote the  $m$ th component of  $\tilde{\mathbf{F}}_1$  and  $\tilde{\mathbf{U}}$  with  $m = 1, \dots, 6$ , respectively.

Solving those linear systems gives  $\tilde{\mathbf{U}}$  and  $\tilde{\mathbf{F}}_1$  as follows

$$\tilde{\mathbf{U}} = \begin{pmatrix} \{z_1\}^{\ln} \\ \{z_2\}^{\ln} \\ \{z_3\} \sum_{\ell=1}^2 \{z_\ell\}^{\ln} \\ \{z_4\} \sum_{\ell=1}^2 \{z_\ell\}^{\ln} \\ \{z_5\} \sum_{\ell=1}^2 \{z_\ell\}^{\ln} \\ \sum_{\ell=1}^2 \left[ \{z_\ell\}^{\ln} \left( \frac{c_{v,\ell}}{\{z_6\}^{\ln}} - \frac{1}{2} \sum_{m=3}^5 \{z_m^2\} \right) \right] + \sum_{\ell=1}^2 \{z_\ell\}^{\ln} \sum_{m=3}^5 \{z_m\}^2 + \sum_{\ell=1}^2 p_{\infty,\ell} \end{pmatrix},$$

$$\tilde{\mathbf{F}}_1 = \begin{pmatrix} \{z_1\}^{\ln} \{z_3\}, \\ \{z_2\}^{\ln} \{z_3\}, \\ \{z_3\} \sum_{\ell=1}^2 \tilde{\mathbf{F}}_{1,\ell} + \frac{1}{\{z_6\}} \left( \sum_{\ell=1}^2 R_\ell \{z_\ell\} \right) - \sum_{\ell=1}^2 p_{\infty,\ell} \\ \{z_4\} \sum_{\ell=1}^2 \tilde{\mathbf{F}}_{1,\ell} \\ \{z_5\} \sum_{\ell=1}^2 \tilde{\mathbf{F}}_{1,\ell} \\ \sum_{\ell=1}^2 \left[ \tilde{\mathbf{F}}_{1,\ell} \left( \frac{c_{v,\ell}}{\{z_6\}^{\ln}} - \frac{1}{2} \sum_{m=3}^5 \{z_m^2\} \right) \right] + \sum_{m=3}^5 \left( \{z_m\} \tilde{\mathbf{F}}_{1,m} \right) + \sum_{\ell=1}^2 p_{\infty,\ell} \{z_3\} \end{pmatrix}.$$

For  $k = 2, 3$ ,  $\tilde{\mathbf{F}}_k$  may be similarly derived. For the entropy pair  $(\eta, q_k)$  in (3.16),  $\tilde{\mathbf{F}}_k$  can also be obtained by choosing respectively the angles  $\varphi = 0, \theta = \pi/2$  and  $\varphi = \pi/2, \theta = 0$  in

$$\tilde{\mathbf{F}}_{\varphi,\theta}(\mathbf{U}_l, \mathbf{U}_r) := \mathbf{T}^{-1} \tilde{\mathbf{F}}_1 \left( \hat{\mathbf{U}}_l, \hat{\mathbf{U}}_r \right), \quad (3.19)$$

which is the EC flux approximating the flux  $\cos \varphi \cos \theta \mathbf{F}_1(\mathbf{U}) + \cos \varphi \sin \theta \mathbf{F}_2(\mathbf{U}) + \sin \varphi \mathbf{F}_3(\mathbf{U})$ , where  $\varphi \in [0, 2\pi)$ ,  $\theta \in [0, \pi]$ ,  $\hat{\mathbf{U}}_l := \mathbf{T}\mathbf{U}_l$ ,  $\hat{\mathbf{U}}_r := \mathbf{T}\mathbf{U}_r$ ,  $\mathbf{T}$  is the expanded rotational matrix defined by

$$\mathbf{T} = \begin{bmatrix} \mathbf{I}_N & 0 & 0 & 0 & 0 \\ 0 & \cos \varphi \cos \theta & \cos \varphi \sin \theta & \sin \varphi & 0 \\ 0 & -\sin \theta & \cos \theta & 0 & 0 \\ 0 & -\sin \varphi \cos \theta & -\sin \varphi \sin \theta & \cos \varphi & 0 \\ 0 & 0 & 0 & 0 & 1 \end{bmatrix}, \quad (3.20)$$

with the unit  $N \times N$  matrix  $\mathbf{I}_N$ ,  $N = 1, 2$ . In fact,  $\tilde{\mathbf{F}}_{\varphi,\theta}(\mathbf{U}_l, \mathbf{U}_r)$  satisfies the sufficient condition of the EC flux

$$\llbracket \mathbf{V}(\mathbf{U}) \rrbracket^T \tilde{\mathbf{F}}_{\varphi,\theta}(\mathbf{U}_l, \mathbf{U}_r) = \cos \varphi \cos \theta \llbracket \psi_1(\mathbf{U}) \rrbracket + \cos \varphi \sin \theta \llbracket \psi_2(\mathbf{U}) \rrbracket + \sin \varphi \llbracket \psi_3(\mathbf{U}) \rrbracket,$$

because

$$\begin{aligned}\widehat{\mathbf{U}} &:= \mathbf{T}\mathbf{U} = (\rho_1, \dots, \rho_N, \hat{v}_1, \hat{v}_2, \hat{v}_3, E)^\top, \quad \hat{v}_1 = \cos \varphi \cos \theta v_1 + \cos \varphi \sin \theta v_2 + \sin \varphi v_3, \\ \hat{v}_2 &= -\sin \theta v_1 + \cos \theta v_2, \quad \hat{v}_3 = -\sin \varphi \cos \theta v_1 - \sin \varphi \sin \theta v_2 + \cos \varphi v_3, \\ \mathbf{V}(\widehat{\mathbf{U}}) &= \left( -S_1 - \frac{|\mathbf{v}|^2}{2T} + c_{v,1}\Gamma_1, \dots, -S_N - \frac{|\mathbf{v}|^2}{2T} + c_{v,N}\Gamma_N, \frac{\hat{v}}{T}, -\frac{1}{T} \right)^\top,\end{aligned}$$

so that one has  $\mathbf{V}(\widehat{\mathbf{U}}) = \mathbf{V}(\mathbf{T}\mathbf{U}) = \mathbf{T}\mathbf{V}(\mathbf{U})$  and

$$\begin{aligned}\llbracket \mathbf{V}(\mathbf{U}) \rrbracket^\top \widetilde{\mathbf{F}}_{\varphi, \theta}(\mathbf{U}_l, \mathbf{U}_r) &= \llbracket \mathbf{V}(\mathbf{U}) \rrbracket^\top \mathbf{T}^{-1} \widetilde{\mathbf{F}}_1(\widehat{\mathbf{U}}_l, \widehat{\mathbf{U}}_r) = \llbracket \mathbf{V}(\widehat{\mathbf{U}}) \rrbracket^\top \widetilde{\mathbf{F}}_1(\widehat{\mathbf{U}}_l, \widehat{\mathbf{U}}_r) \\ &\stackrel{(3.12)}{=} \llbracket \psi_1(\widehat{\mathbf{U}}) \rrbracket = \llbracket \sum_{\ell=1}^N \left( R_\ell \rho_\ell - \frac{p_{\infty, \ell}}{T} \right) \hat{v}_1 \rrbracket \\ &= \cos \varphi \cos \theta \llbracket \psi_1(\mathbf{U}) \rrbracket + \cos \varphi \sin \theta \llbracket \psi_2(\mathbf{U}) \rrbracket + \sin \varphi \llbracket \psi_3(\mathbf{U}) \rrbracket.\end{aligned}$$

### 3.4. ES schemes

It is known that the EC schemes work well for the smooth solutions, but they may produce severe nonphysical oscillations if the solutions contain discontinuities. In order to suppress those numerical oscillations, a suitable dissipation term should be added to the EC flux (3.6) to make the schemes satisfy the semi-discrete entropy inequality for the given entropy pair. Similar to [14], the high-order accurate ES flux may be given by

$$\left( \widehat{\mathbf{F}}_k \right)_{i,k,\pm\frac{1}{2}} = \left( \widehat{\mathbf{F}}_k \right)_{i,k,\pm\frac{1}{2}}^{2\text{wth}} - \frac{1}{2} \left( \mathbf{T}^{-1} \mathbf{R}(\mathbf{T}\mathbf{U}) \left| \widetilde{\boldsymbol{\Lambda}}(\mathbf{T}\mathbf{U}) \right| \right)_{i,k,\pm\frac{1}{2}} \mathbf{Y}_{i,k,\pm\frac{1}{2}} \llbracket \mathbf{W} \rrbracket_{i,k,\pm\frac{1}{2}}^{\text{WENOMR}}, \quad (3.21)$$

where  $\left| \widetilde{\boldsymbol{\Lambda}}(\mathbf{T}\mathbf{U}) \right| := \max_m \left\{ \left| J \frac{\partial \xi_k}{\partial t} + L_k \lambda_m(\mathbf{T}\mathbf{U}) \right| \right\} \mathbf{I}$ ,  $L_k = \sqrt{\sum_{j=1}^3 \left( J \frac{\partial \xi_k}{\partial x_j} \right)^2}$ , the rotational matrix  $\mathbf{T}$  is given in (3.20) with

$$\begin{aligned}\theta &= \arctan \left( \left( J \frac{\partial \xi_k}{\partial x_2} \right) / \left( J \frac{\partial \xi_k}{\partial x_1} \right) \right), \\ \varphi &= \arctan \left( \left( J \frac{\partial \xi_k}{\partial x_3} \right) / \sqrt{\left( J \frac{\partial \xi_k}{\partial x_1} \right)^2 + \left( J \frac{\partial \xi_k}{\partial x_2} \right)^2} \right),\end{aligned}$$

and  $\mathbf{R}$  is the scaled right eigenvector matrix satisfying

$$\frac{\partial \mathbf{U}}{\partial \mathbf{V}} = \mathbf{R} \mathbf{R}^\top, \quad \frac{\partial \mathbf{F}_1}{\partial \mathbf{U}} = \mathbf{R} \boldsymbol{\Lambda} \mathbf{R}^{-1}, \quad (3.22)$$

here  $\boldsymbol{\Lambda}$  is the diagonal matrix, whose diagonal elements are the eigenvalues of the matrix  $\frac{\partial \mathbf{F}_1}{\partial \mathbf{U}}$ . The high-order accurate jump terms in (3.21) are defined as  $\llbracket \mathbf{W} \rrbracket_{i,k,\pm\frac{1}{2}}^{\text{WENOMR}} := \mathbf{W}_{i,k,\pm\frac{1}{2}}^{\text{WENOMR},+} - \mathbf{W}_{i,k,\pm\frac{1}{2}}^{\text{WENOMR},-}$  with

the left and right limit values  $\mathbf{W}_{i,k,\pm\frac{1}{2}}^{\text{WENOMR},-}$  and  $\mathbf{W}_{i,k,\pm\frac{1}{2}}^{\text{WENOMR},+}$  obtained by the high-order multi-resolution WENO reconstruction [49]. The diagonal matrix  $\mathbf{Y}_{i,k,\pm\frac{1}{2}}$  is chosen as

$$(\mathbf{Y}_{m,m})_{i,k,\pm\frac{1}{2}} = \begin{cases} 1, & \text{if } \text{sign}\left(\llbracket \mathbf{W}_m \rrbracket_{i,k,\pm\frac{1}{2}}^{\text{WENOMR}}\right) \text{sign}\left(\llbracket \mathbf{W}_m \rrbracket_{i,k,\pm\frac{1}{2}}\right) > 0, \\ 0, & \text{otherwise,} \end{cases}$$

in order to ensure the ‘‘sign’’ property [2].

**Remark 3.2.** Our computations will take the fifth-order multi-resolution WENO reconstruction, which uses unequal-sized stencils and arbitrary positive linear weights whose sum is one [49], see [Appendix A](#). The ES adaptive moving mesh schemes based on the multi-resolution WENO reconstruction can better capture the localized structures for the (multi-component) flow problems, and outperform their counterparts based on the classical WENO reconstruction [28] with a slight increase in the computational cost, see [Section 5](#).

Before ending this section, we give the scaled eigenvector matrix  $\mathbf{R}$  for the multi-component compressible Euler equations ( $N = 1, 2$ ) with the stiffened EOS.

For the single-component compressible Euler equations ( $N = 1$ ), the diagonal matrix  $\mathbf{\Lambda}$  is given by

$$\mathbf{\Lambda} = \text{diag}\{\lambda_1, \dots, \lambda_5\} = \text{diag}\{v_1 - c_s, v_1, v_1, v_1, v_1 + c_s\},$$

where  $c_s$  is the speed of sound given by  $c_s^2 = R_1\Gamma_1T$ . After some algebraic manipulations, the scaled eigenvector matrix  $\mathbf{R}$  can be expressed as

$$\begin{bmatrix} 1 & 1 & 0 & 0 & 1 \\ v_1 - c_s & v_1 & 0 & 0 & v_1 + c_s \\ v_2 & v_2 & 1 & 0 & v_2 \\ v_3 & v_3 & 0 & 1 & v_3 \\ H - c_s v_1 & \frac{1}{2}|\mathbf{v}|^2 & v_2 & v_3 & H + c_s v_1 \end{bmatrix} \begin{bmatrix} \frac{\rho_1}{2\Gamma_1 R_1} & 0 & 0 & 0 & 0 \\ 0 & \frac{\rho_1}{c_{v,1}\Gamma_1} & 0 & 0 & 0 \\ 0 & 0 & \rho_1 T & 0 & 0 \\ 0 & 0 & 0 & \rho_1 T & 0 \\ 0 & 0 & 0 & 0 & \frac{\rho_1}{2\Gamma_1 R_1} \end{bmatrix}^{\frac{1}{2}},$$

where  $H = (E + p)/\rho_1$  is the total enthalpy. In practice, the values of  $\mathbf{R}_{i,k,\pm\frac{1}{2}}$  and  $\left|\tilde{\mathbf{\Lambda}}\right|_{i,k,\pm\frac{1}{2}}$  are calculated by using some ‘‘averaged’’ values of the primitive variables as follows

$$\bar{\rho}_1 = \{\{\rho_1\}\}_{i,k,\pm\frac{1}{2}}^{\ln}, \quad \bar{\mathbf{v}} = \{\{\mathbf{v}\}\}_{i,k,\pm\frac{1}{2}}, \quad \bar{p} + p_{\infty,1} = \left(\frac{\{\{\rho_1\}\}^{\ln}}{\{\{\rho_1/(p + p_{\infty,1})\}\}^{\ln}}\right)_{i,k,\pm\frac{1}{2}}.$$

For the two-component compressible Euler equations ( $N = 2$ ) with the stiffened EOS, utilizing the similar procedure for the ideal EOS in [23], the diagonal matrix is given by

$$\mathbf{\Lambda} = \text{diag}\{\lambda_1, \dots, \lambda_6\} = \text{diag}\{v_1 - c_s, v_1, v_1, v_1, v_1, v_1 + c_s\},$$

where  $c_s^2 = R\Gamma T$  with  $R := (\sum (\Gamma_\ell - 1) c_{v,\ell} \rho_\ell) / \sum \rho_\ell$ . The scaled eigenvector matrix  $\mathbf{R}$  can be obtained by scaling the right eigenvectors  $\tilde{\mathbf{R}}$  using a symmetric block diagonal matrix  $\mathbf{D}$ , i.e.  $\mathbf{R} = \tilde{\mathbf{R}}\mathbf{D}$ , where  $\tilde{\mathbf{R}}$  is

$$\begin{bmatrix} Y_1 & 1 & 0 & 0 & 0 & Y_1 \\ Y_2 & 0 & 1 & 0 & 0 & Y_2 \\ v_1 - c_s & v_1 & v_1 & 0 & 0 & v_1 + c_s \\ v_2 & v_2 & v_2 & c_s & 0 & v_2 \\ v_3 & v_3 & v_3 & 0 & c_s & v_3 \\ H - c_s v_1 & \frac{1}{2}|\mathbf{v}|^2 - \frac{d_1}{\Gamma - 1} & \frac{1}{2}|\mathbf{v}|^2 - \frac{d_2}{\Gamma - 1} & c_s v_2 & c_s v_3 & H + c_s v_1 \end{bmatrix},$$

where  $d_\ell = h_\ell - \Gamma c_{v,\ell} T$ , and  $H = \sum \rho_\ell h_\ell / \rho + \frac{1}{2}|\mathbf{v}|^2$  with  $h_\ell := c_{v,\ell} T + R_\ell T$ . According to (3.22), the explicit expression for the matrix  $\mathbf{D}\mathbf{D}^T$  is provided by

$$\begin{aligned} \mathbf{D}\mathbf{D}^T &= \tilde{\mathbf{R}}^{-1} \frac{\partial \mathbf{U}}{\partial \mathbf{V}} \tilde{\mathbf{R}}^{-T} = \frac{\rho}{\Gamma R} \text{diag} (1/2, \mathbf{D}^{2Y}, 1, 1, 1/2), \\ \mathbf{D}^{2Y} &:= Y_1 Y_2 \begin{bmatrix} (\Gamma - 1)Y_1/Y_2 + (\Gamma R_2/R_1) & -1 \\ -1 & (\Gamma - 1)Y_2/Y_1 + (\Gamma R_1/R_2) \end{bmatrix}, \end{aligned}$$

with  $Y_\ell = \rho_\ell / \rho$ . If decomposing  $\mathbf{D}^{2Y}$  as

$$\mathbf{D}^{2Y} = \mathbf{D}^Y (\mathbf{D}^Y)^T, \quad \mathbf{D}^Y := \sqrt{Y_1 Y_2} \begin{bmatrix} -\sqrt{\Gamma R_2/R_1} & \sqrt{(\Gamma - 1)Y_1/Y_2} \\ \sqrt{\Gamma R_1/R_2} & \sqrt{(\Gamma - 1)Y_2/Y_1} \end{bmatrix},$$

then  $\mathbf{D} = \frac{\sqrt{\rho}}{\sqrt{\Gamma R}} \text{diag} (1/\sqrt{2}, \mathbf{D}^Y, 1, 1, 1/\sqrt{2})$ . Thus the scaled eigenvector matrix  $\mathbf{R}$  is obtained by

$$\tilde{\mathbf{R}} \times \sqrt{\frac{\rho}{\Gamma R}} \begin{bmatrix} \frac{1}{\sqrt{2}} & 0 & 0 & 0 & 0 & 0 \\ 0 & -\sqrt{Y_1 Y_2} \sqrt{\Gamma R_2/R_1} & Y_1 \sqrt{\Gamma - 1} & 0 & 0 & 0 \\ 0 & \sqrt{Y_1 Y_2} \sqrt{\Gamma R_1/R_2} & Y_2 \sqrt{\Gamma - 1} & 0 & 0 & 0 \\ 0 & 0 & 0 & 1 & 0 & 0 \\ 0 & 0 & 0 & 0 & 1 & 0 \\ 0 & 0 & 0 & 0 & 0 & \frac{1}{\sqrt{2}} \end{bmatrix}.$$

Similarly, the values of  $\mathbf{R}_{i,k,+1/2}$  and  $|\tilde{\mathbf{\Lambda}}|_{i,k,+1/2}$  are calculated by using some averaged values at  $\{i, k, +1/2\}$

$$\begin{aligned} \bar{\rho}_1 &= \{\{\rho_1\}\}^{\text{ln}}, \quad \bar{\rho}_2 = \{\{\rho_2\}\}^{\text{ln}}, \quad \bar{\rho} = \{\{\rho\}\}^{\text{ln}}, \quad \bar{\mathbf{v}} = \{\{\mathbf{v}\}\}, \quad \bar{T} = 1/\{\{1/T\}\}^{\text{ln}}, \\ \bar{R} &= \{\{R\}\}, \quad \bar{\Gamma} = \{\{\Gamma\}\}, \quad \sum_{\ell=1}^2 \bar{\rho}_\ell \bar{h}_\ell = \sum_{\ell=1}^2 (c_{v,\ell} \bar{\rho}_\ell \bar{T} + p_{\infty,\ell}) + \{\{p\}\}. \end{aligned}$$

#### 4. Adaptive moving mesh strategy

This section introduces the adaptive moving mesh strategy [14], but will omit the dependence of the variables on  $t$  for convenience, unless otherwise stated.

The mesh is moved adaptively, which is equivalent to finding the coordinate transformation  $\mathbf{x} = \mathbf{x}(\boldsymbol{\xi})$  from  $\Omega_c$  to  $\Omega_p$  mentioned in Section 2. Such transformation can be obtained by solving the mesh redistribution equations

$$\nabla_{\boldsymbol{\xi}} \cdot (\mathbf{G}_k \nabla_{\boldsymbol{\xi}} x_k) = 0, \quad \boldsymbol{\xi} \in \Omega_c, \quad k = 1, 2, 3, \quad (4.1)$$

which may be the Euler-Lagrange equations or the stationary variational conditions for minimizing the mesh adaptation functional, where  $\mathbf{G}_k$  is the symmetric positive definite matrix depending on the solutions of the underlying governing equations (1.1) or their derivatives. The simplest choice of  $\mathbf{G}_k$  is

$$\mathbf{G}_k = \Theta \mathbf{I}_3,$$

where the monitor function  $\Theta$  is positive and taken in this paper as

$$\Theta = \left( 1 + \sum_{k=1}^{\kappa} \alpha_k \left( \frac{|\nabla_{\boldsymbol{\xi}} \sigma_k|}{\max |\nabla_{\boldsymbol{\xi}} \sigma_k|} \right)^2 \right)^{1/2}, \quad (4.2)$$

here  $\sigma_k$  is a physical variable,  $\alpha_k$  is a non-negative parameter, and  $\kappa$  is the number of the chosen physical variables. Using the second-order accurate central difference scheme and the Jacobi iteration, the mesh equations (4.1) are approximated by

$$\sum_{k=1}^d \left[ \Theta_{i,k,+\frac{1}{2}} \left( \mathbf{x}_{i,k,1}^{[\nu]} - \mathbf{x}_i^{[\nu+1]} \right) - \Theta_{i,k,-\frac{1}{2}} \left( \mathbf{x}_i^{[\nu+1]} - \mathbf{x}_{i,k,-1}^{[\nu]} \right) \right] / \Delta \xi_k^2 = 0, \quad \nu = 0, 1, \dots, \mu,$$

where  $\mathbf{x}_i^{[0]} := \mathbf{x}_i^n$ , and  $\Theta_{i,k,\pm\frac{1}{2}} := \frac{1}{2} (\Theta_{i,k} + \Theta_{i,k,\pm 1})$ . The total iteration number  $\mu$  is taken as 10 in our numerical tests. The final adaptive mesh is given by  $\mathbf{x}_i^{n+1} := \mathbf{x}_i^n + \Delta_{\tau} (\delta_{\tau} \mathbf{x})_i^n$ , where  $(\delta_{\tau} \mathbf{x})_i^n := \mathbf{x}_i^{[\mu]} - \mathbf{x}_i^n$ , and the parameter  $\Delta_{\tau}$  is the limiter of the movement of mesh points satisfying

$$\Delta_{\tau} \leq \begin{cases} -\frac{1}{2(\delta_{\tau} x_k)_i^n} \left[ (x_k)_i^n - (x_k)_{i,k,-1}^n \right], & (\delta_{\tau} x_k)_i^n < 0, \\ \frac{1}{2(\delta_{\tau} x_k)_i^n} \left[ (x_k)_{i,k,+1}^n - (x_k)_i^n \right], & (\delta_{\tau} x_k)_i^n > 0, \end{cases} \quad k = 1, \dots, d.$$

Finally, the mesh velocity at  $t = t_n$  in (3.10) is determined by  $\dot{\mathbf{x}}_i^n := \Delta_{\tau} (\delta_{\tau} \mathbf{x})_i^n / \Delta t_n$  with the time stepsize  $\Delta t_n$ , obtained by (5.1) in Section 5.

**Remark 4.1.** In order to weaken the singularity of the monitor function near the strong discontinuity, it is useful to apply the following low pass filter

$$\Theta_{i_1, i_2, i_3} \leftarrow \sum_{j_1, j_2, j_3=0, \pm 1} \left( \frac{1}{2} \right)^{|j_1|+|j_2|+|j_3|+3} \Theta_{i_1+j_1, i_2+j_2, i_3+j_3},$$

to smooth the monitor function 3 ~ 10 times.



## 5. Numerical results

This section conducts several 2D and 3D numerical tests to validate the accuracy and the ability in capturing the localized structures of the previous fifth-order adaptive moving mesh methods. The fully-discrete schemes are derived by using the third-order accurate explicit SSP RK time discretization [22], and implemented in parallel with the MPI parts of the PLUTO code [34]. All computations are performed on the CPU nodes of the High-performance Computing Platform of Peking University (Linux Redhat environment, two Intel Xeon E5-2697A V4 per node, and core frequency of 2.6GHz). The time stepsize  $\Delta t_n$  is determined by the CFL condition

$$\Delta t_n \leq \frac{C_{\text{CFL}}}{\max_i \left\{ \sum_{k=1}^3 \varrho_{i,k}^n / \Delta \xi_k \right\}}, \quad (5.1)$$

but it will be taken as  $C_{\text{CFL}}(\min \Delta \xi_k)^{5/3}$  in all accuracy tests in order to make the spatial error dominant, where  $\varrho_{i,k}$  is the spectral radius of the eigen-matrix in the  $\xi_k$ -direction, and  $C_{\text{CFL}}$  is taken as 0.4 and 0.3 in 2D and 3D examples, respectively, unless otherwise stated. For the sake of convenience, the fully-discrete fifth-order finite difference schemes with the multi-resolution WENO reconstruction and the ES fluxes on the uniform and moving meshes are denoted by “UM-WENOMR” and “MM-WENOMR”, respectively. For a comparison, the counterparts of “MM-WENOMR” with the classical WENO reconstruction [28] denoted by “MM-WENOJS” are also implemented.

### 5.1. Single-component compressible Euler equations ( $N = 1$ )

This section considers some numerical experiments on the 2D and 3D single-component compressible Euler equations ( $N = 1$ ) with the ideal and stiffened EOS. The adiabatic index  $\Gamma_1$  and the specific heat at constant volume  $c_{v,1}$  are respectively taken as 1.4 and 1, unless otherwise stated.

**Example 5.1** (2D isentropic vortex). This example is to test the accuracy of MM-WENOMR by solving the problem describing an isentropic vortex propagating periodically at a constant speed in the 2D domain  $\Omega_p = [-10, 10]^2$ . Initially, the domain is divided into uniformly  $N_1 \times N_1$  rectangular cells, and the vortex perturbation

$$(\delta v_1, \delta v_2) = \frac{\epsilon}{2\pi} e^{0.5(1-r^2)} ((x_2 + 2), -(x_1 + 2)), \quad \delta T = -\frac{\epsilon^2}{8\Gamma_1 \pi^2} e^{(1-r^2)}, \quad \delta S_1 = 0,$$

is added to the mean flow  $\rho_1 = 1$ ,  $T = 1$  and  $(v_1, v_2) = (1, 1)$ , where  $p_{\infty,1} = 0$ ,  $r^2 = (x_1 + 2)^2 + (x_2 + 2)^2$  with the vortex strength  $\epsilon = 5$ . The monitor function is chosen as

$$\Theta = \left( 1 + \frac{20|\nabla_{\xi} \rho_1|}{\max |\nabla_{\xi} \rho_1|} + \frac{10|\Delta_{\xi} \rho_1|}{\max |\Delta_{\xi} \rho_1|} \right)^{1/2}.$$

Figure 5.1 presents the adaptive mesh with  $N_1 = 80$  and the density contours (10 equally spaced contour lines) at  $t = 0, 2, 4$ . Figure 5.2 shows the  $\ell^1$ - and  $\ell^\infty$ -errors in  $\rho_1$  at  $t = 4$  versus

$N_1$ , the orders of convergence and the discrete total entropy  $\sum_{i_1, i_2} J_{i_1, i_2} \eta(\mathbf{U}_{i_1, i_2}) \Delta \xi_1 \Delta \xi_2$  with respect to time by using the EC and ES schemes with  $N_1 = 160$ , respectively. It is easy to see that the mesh points well and adaptively concentrate near the large gradient area of the density as expected, MM-WENOMR gets the fifth-order accuracy, and the EC scheme almost keeps the total entropy conservative, while the total entropy of the ES scheme decays in time.

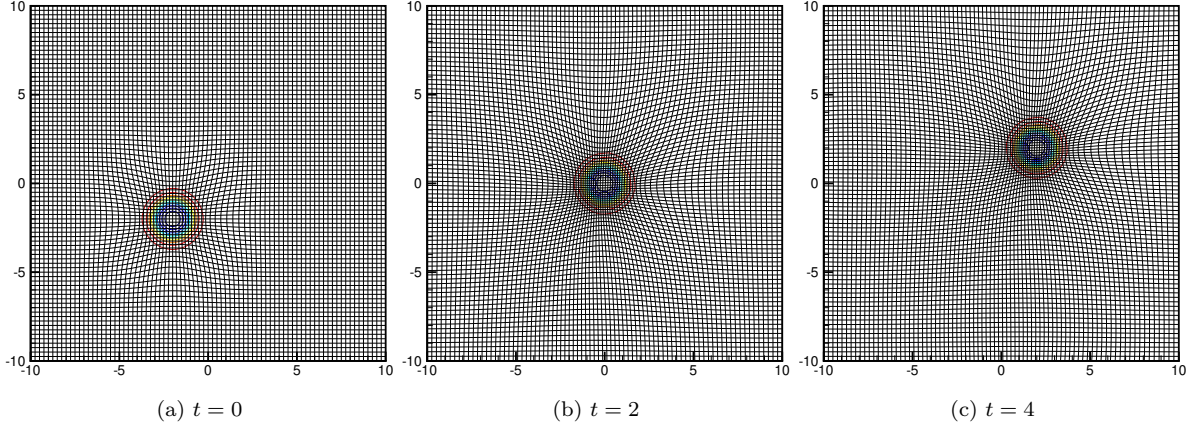


Figure 5.1: Example 5.1. Adaptive meshes and density contours at  $t = 0, 2, 4$  with  $80 \times 80$  cells.

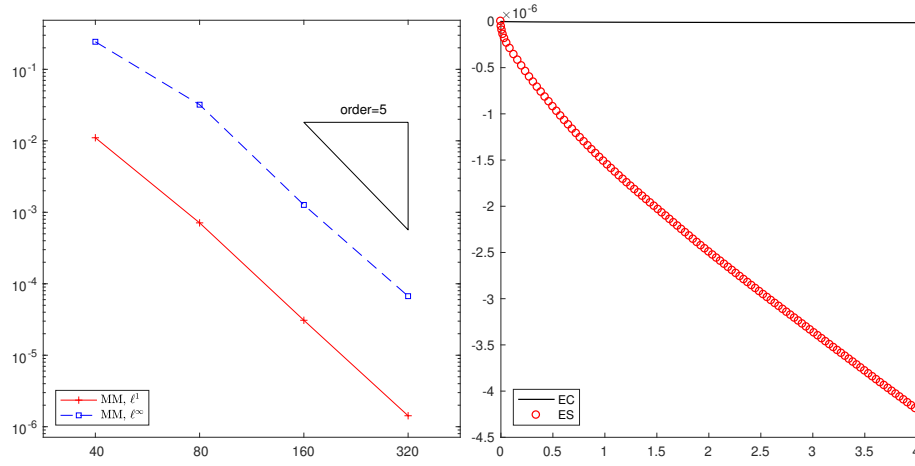


Figure 5.2: Example 5.1. Left:  $\ell^1$ - and  $\ell^\infty$ -errors in  $\rho_1$  at  $t = 4$  versus  $N_1$  and orders of convergence; right: total entropy with respect to  $t$  with  $N_1 = 160$ .

**Example 5.2** (Quasi 2D shock tube). The initial data are

$$(\rho_1, v_1, v_2, p) = \begin{cases} (1, 0, 0, 1), & x_1 < 0.5, \\ (0.75, 0, 0, 0.05), & x_1 > 0.5, \end{cases}$$

with  $p_{\infty, 1} = 1$  and  $\Gamma_1 = 3$ , see [51]. The exact solution consists of a narrow rarefaction wave, a contact discontinuity and a right moving shock wave. The monitor function is chosen as (4.2) with  $\kappa = 1, \sigma_1 = \rho_1$  and  $\alpha_1 = 1200$ .

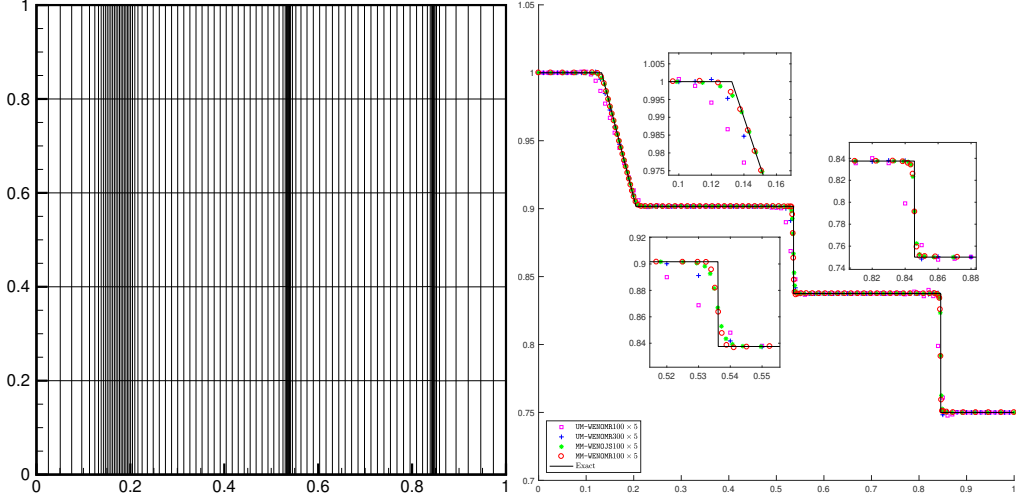


Figure 5.3: Example 5.2. Adaptive mesh of  $100 \times 5$  cells (Left) and densities (Right) at  $t = 0.15$ .

	MM-WENOMR	MM-WENOJS	UM-WENOMR	UM-WENOMR
Example 5.3	2m56s ( $200 \times 200$ cells)	2m37s ( $200 \times 200$ cells)	28s ( $200 \times 200$ cells)	7m9s ( $500 \times 500$ cells)
Example 5.4	2m50s ( $200 \times 200$ cells)	2m38s ( $200 \times 200$ cells)	36s ( $200 \times 200$ cells)	13m10s ( $600 \times 600$ cells)

Table 5.1: CPU times of Examples 5.3-5.4 (4 cores).

Figure 5.3 shows the adaptive mesh and the densities at  $t = 0.15$  obtained respectively by the schemes on the adaptive moving mesh and the uniform mesh. We see that the mesh points adaptively concentrate near the large gradient area of the density, and MM-WENOMR with  $N_1 = 100$  is superior to UM-WENOMR with  $N_1 = 100$ , better than MM-WENOJS with  $N_1 = 100$  near the contact discontinuity and UM-WENOMR with  $N_1 = 300$  near the head of the rarefaction wave, the contact discontinuity.

**Example 5.3** (2D Riemann problem I). The initial data are [6]

$$(\rho_1, v_1, v_2, p) = \begin{cases} (0.5313, 0, 0, 0.4), & x_1 > 0.5, x_2 > 0.5, \\ (1, 0.7276, 0, 1), & x_1 < 0.5, x_2 > 0.5, \\ (0.8, 0, 0, 1), & x_1 < 0.5, x_2 < 0.5, \\ (1, 0, 0.7276, 1), & \text{otherwise,} \end{cases}$$

with  $p_{\infty,1} = 0$ . The initial discontinuities are two shock waves and two contact discontinuities.

The monitor function is the same as that used in Example 5.2, and the linear weights of the multi-resolution WENO reconstruction are taken as  $\chi_1 = 0.95, \chi_2 = 0.045$  and  $\chi_3 = 0.005$ . Figure 5.4 gives the adaptive mesh of MM-WENOMR with  $200 \times 200$  cells, the density contours (40 equally spaced contour lines) and the densities along  $x_1 = x_2$  at  $t = 0.25$ . The schemes can capture important flow structures such as the Mach reflection resulting from the initial two shock waves

and the following emerged jet moving towards the lower left direction near the center of the domain. One can see that MM-WENOMR with  $200 \times 200$  cells gives sharper transitions near the shock waves than UM-WENOMR with  $500 \times 500$  cells and MM-WENOJS with  $200 \times 200$  cells, and the resolution of MM-WENOMR is better than MM-WENOJS, see Figure 5.4f, although its CPU time is slightly larger than MM-WENOJS, see Table 5.1. From Table 5.1, we can also see that MM-WENOMR only takes 41.0% CPU time of UM-WENOMR with  $500 \times 500$  cells, showing the high efficiency of the adaptive moving mesh scheme.

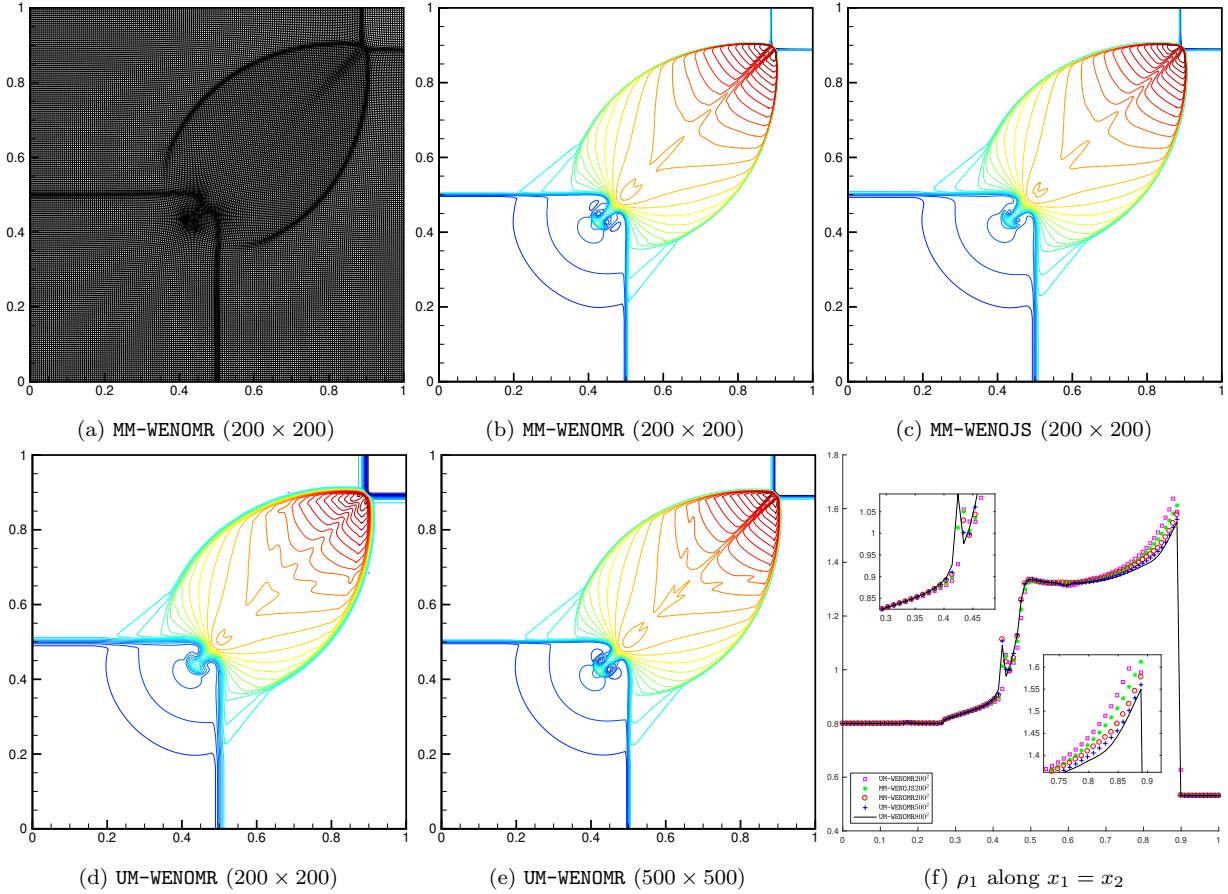


Figure 5.4: Example 5.3. Adaptive mesh of MM-WENOMR with  $200 \times 200$  cells, density contours (40 equally spaced contour lines) of MM-WENOMR, MM-WENOJS, and UM-WENOMR, and densities along  $x_1 = x_2$  at  $t = 0.25$ .

**Example 5.4** (2D Riemann problem II). The initial data are [31]

$$(\rho_1, v_1, v_2, p) = \begin{cases} (1, 0.75, -0.5, 1), & x_1 > 0.5, x_2 > 0.5, \\ (2, 0.75, 0.5, 1), & x_1 < 0.5, x_2 > 0.5, \\ (1, -0.75, 0.5, 1), & x_1 < 0.5, x_2 < 0.5, \\ (3, -0.75, -0.5, 1), & \text{otherwise,} \end{cases}$$

with  $p_{\infty,1} = 0$ . It describes the interaction of four contact discontinuities.

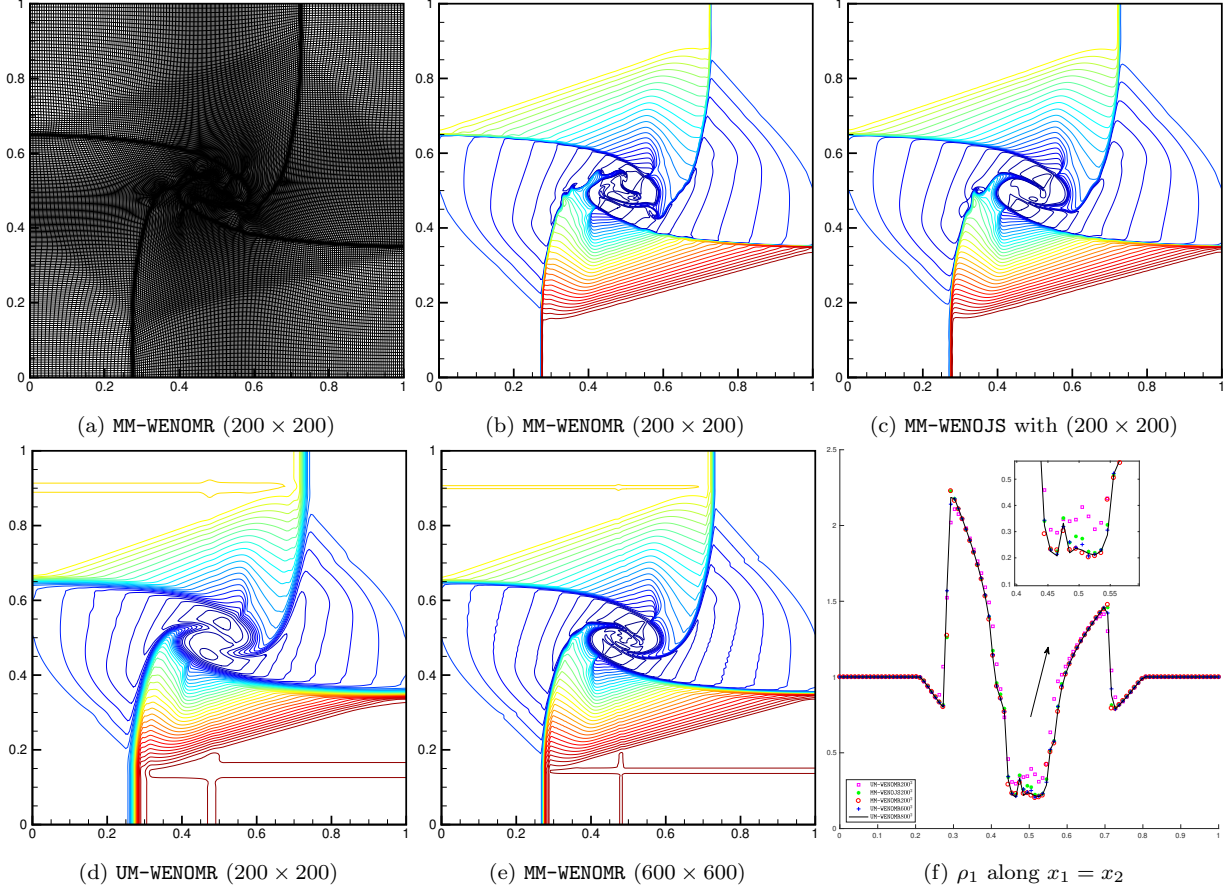


Figure 5.5: Example 5.4. Adaptive mesh of MM-WENOMR with  $200 \times 200$  cells, density contours (40 equally spaced contour lines) of MM-WENOMR, MM-WENOJS, and UM-WENOMR, and densities along  $x_1 = x_2$  at  $t = 0.3$ .

The monitor function and the linear weights of the multi-resolution WENO reconstruction are the same as those used in Example 5.2. Figure 5.5 shows the adaptive mesh of MM-WENOMR with  $200 \times 200$  cells and the densities at  $t = 0.3$ . It is seen that the four initial contact discontinuities interact with each other to form a spiral with the low density around the center of the domain as time increases. The moving mesh methods capture the contact discontinuities and the rarefaction wave well, and MM-WENOMR displays more small scale structures and roll up of the slip lines than UM-WENOMR with  $600 \times 600$  cells and MM-WENOJS with  $200 \times 200$  cells. The CPU times in Table 5.1 clearly highlight the efficiency of MM-WENOMR, which takes only 21.5% CPU time of UM-WENOMR with  $600 \times 600$  cells and 7.6% time more than MM-WENOJS with  $200 \times 200$  cells.

**Example 5.5 (3D isentropic vortex).** This example is to check the accuracy of the 3D ES adaptive moving mesh method via the 3D isentropic vortex problem describing a smooth isentropic vortex moving in a certain direction. The initial data are similar to that in [3] except for that the cylindrical

vortex is rotated to the diagonal of the domain  $\Omega_p = [-10, 10]^3$ , given by

$$T = 1 - \frac{\epsilon^2}{8\Gamma_1\pi^2}e^{1-r^2}, \quad \rho_1 = T^{1/(\Gamma_1-1)}, \quad p = (\Gamma_1 - 1)\rho_1 T,$$

$$\mathbf{v} = \frac{1}{\sqrt{6}} \left( \tilde{v}_1 - \sqrt{3}\tilde{v}_2 + \sqrt{2}, \tilde{v}_1 + \sqrt{3}\tilde{v}_2 + \sqrt{2}, -2\tilde{v}_1 + \sqrt{2} \right)^T,$$

where

$$p_{\infty,1} = 0, \quad c_{v,1} = 1, \quad \epsilon = 5, \quad r^2 = \tilde{x}_1^2 + \tilde{x}_2^2,$$

$$(\tilde{x}_1, \tilde{x}_2) = \frac{1}{\sqrt{6}}(\hat{x}_1 + 2\hat{x}_2, \sqrt{3}\hat{x}_1), \quad (\tilde{v}_1, \tilde{v}_2) = (1, 1) + \frac{\epsilon}{2\pi}e^{\frac{1-r^2}{2}}(\tilde{x}_2, -\tilde{x}_1),$$

$$(\hat{x}_1, \hat{x}_2) = (-x_1 + x_2 + 20k_1, x_1 - x_3 + 20k_2), \quad (\hat{x}_1, \hat{x}_2) \in [-10, 10]^2, \quad k_1, k_2 \in \mathbb{Z}.$$

Figure 5.6 shows the  $\ell^1$ - and  $\ell^\infty$ -errors in  $\rho_1$  at  $t = 0.1$ , the orders of convergence obtained by using MM-WENOMR, and the time-evolutions of the discrete total entropy  $\sum_i J_i \eta(\mathbf{U}_i) \Delta\xi_1 \Delta\xi_2 \Delta\xi_3$  obtained by the EC adaptive moving mesh scheme and MM-WENOMR. The monitor function is the same as that used in Example 5.1, and the boundary points move adaptively according to the periodic boundary conditions. The results show that MM-WENOMR can achieve the expected convergence orders, and the EC scheme almost keeps the total entropy conservative whereas the total entropy of the ES scheme decays in time.

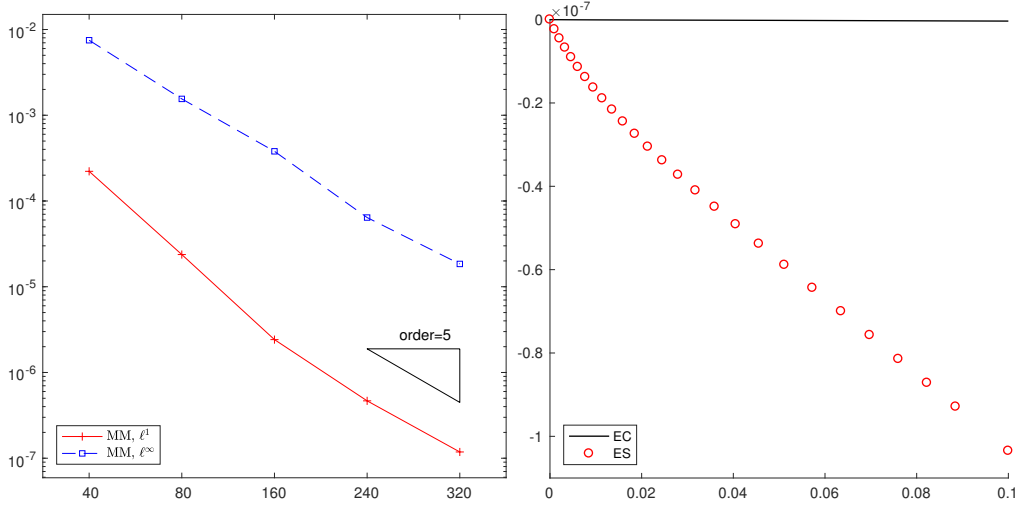


Figure 5.6: Example 5.5. Left:  $\ell^1$ - and  $\ell^\infty$ -errors in  $\rho_1$  at  $t = 0.1$  and the orders of convergence; right: the total entropy with respect to  $t$  with  $N_1 = 160$ .

**Example 5.6** (3D spherical symmetric shock tube). The initial data are

$$(\rho_1, v_1, v_2, v_3, p) = \begin{cases} (1.0, 0, 0, 0, 1.0), & \sqrt{x_1^2 + x_2^2 + x_3^2} < 0.5, \\ (0.125, 0, 0, 0, 0.1), & \text{otherwise,} \end{cases}$$

	MM-WENOMR	MM-WENOJS	UM-WENOMR	UM-WENOMR
Example 5.6	13m53s (100 <sup>3</sup> cells)	13m52s (100 <sup>3</sup> cells)	2m45s (100 <sup>3</sup> cells)	37m19s (200 <sup>3</sup> cells)
Example 5.7	3m21s (350 × 150 cells)	3m3s (350 × 150 cells)	49s (350 × 150 cells)	18m7s (1050 × 450 cells)

Table 5.2: CPU times of Examples 5.6-5.7 (32 cores).

with  $p_{\infty,1} = 0$ , and the domain  $\Omega_p$  is taken as  $[0, 1]^3$ . The monitor function is chosen as (4.2) with  $\kappa = 1, \sigma_1 = \rho_1$  and  $\alpha_1 = 500$ . Figure 5.7a shows that the mesh points adaptively concentrate near the large gradient area of the density. Figure 5.7b gives the densities  $\rho_1$  along the line connecting  $(0, 0, 0)$  and  $(1, 1, 1)$ , where the solid line denotes the reference solution obtained by a second-order TVD scheme using uniform mesh of 8000 cells in the 1D spherical coordinates. It is seen that MM-WENOMR with 100<sup>3</sup> cells is better than UM-WENOMR with 100<sup>3</sup> cells near the rarefaction wave, the contact discontinuity and the shock wave, and the adaptive moving mesh method can precisely capture the flow features. Table 5.2 shows that MM-WENOMR with 100<sup>3</sup> cells only takes 37.2% CPU time of UM-WENOMR with 200<sup>3</sup> cells, but it gives comparable results, verifying the efficiency of MM-WENOMR, and the solution of MM-WENOMR with 100<sup>3</sup> cells is as good as that of MM-WENOJS with comparable CPU time.

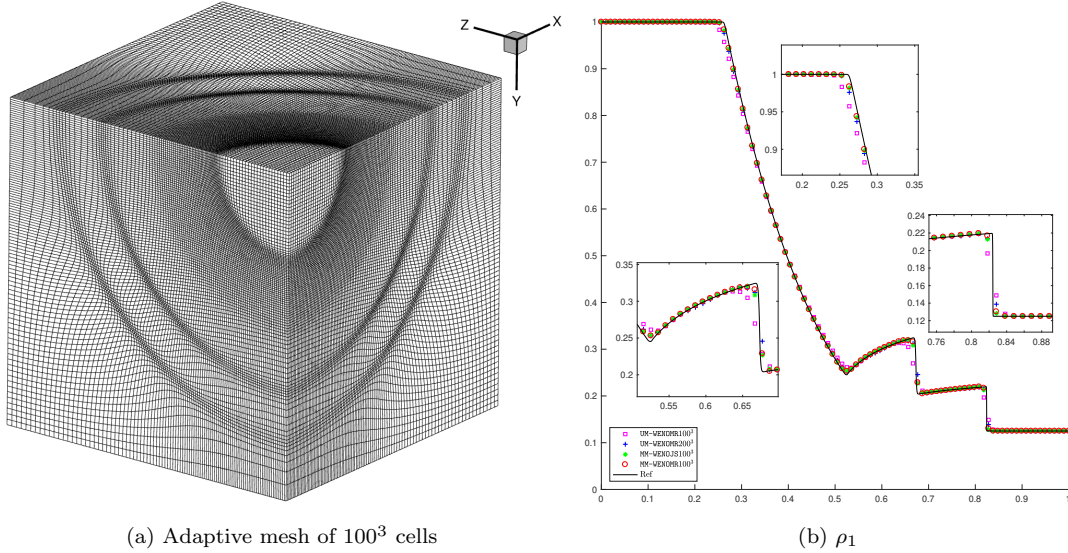


Figure 5.7: Example 5.6. Adaptive mesh of MM-WENOMR and  $\rho_1$  along the line connecting  $(0, 0, 0)$  and  $(1, 1, 1)$  at  $t = 0.2$ .

## 5.2. Two-component compressible Euler equations ( $N = 2$ )

This section solves the 2D and 3D two-component compressible Euler equations ( $N = 2$ ) with the ideal and stiffened EOS.

**Example 5.7** (2D tri-point problem). It corresponds to a 2D three-state Riemann problem in a rectangular domain  $\Omega_p$ , illustrated in Figure 5.8, and has been widely used in testing the high-resolution numerical schemes [20]. Initially,  $\Omega_p = [0, 7] \times [0, 3]$  is split into three sub-domains  $\Omega_1 = [0, 1] \times [0, 3]$ ,  $\Omega_2 = [1, 7] \times [1.5, 3]$ , and  $\Omega_3 = [1, 7] \times [0, 1.5]$ , and the initial data are

$$(\rho_1, \rho_2, v_1, v_2, p) = \begin{cases} (1 - \epsilon, \epsilon, 0, 0, 1), & (x_1, x_2) \in \Omega_1, \\ (0.125 - \epsilon, \epsilon, 0, 0, 0.1), & (x_1, x_2) \in \Omega_2, \\ (\epsilon, 1 - \epsilon, 0, 0, 0.1), & (x_1, x_2) \in \Omega_3, \end{cases}$$

where  $\epsilon = 10^{-5}$ ,  $\Gamma_1 = 1.5$ ,  $\Gamma_2 = 1.4$ ,  $p_{\infty,1} = p_{\infty,2} = 0$ , and  $c_{v,1} = c_{v,2} = 1$ .

The adaptive meshes and densities at  $t = 3.5$  and 5 are plotted in Figures 5.9 and 5.10, where the monitor function is chosen as (4.2) with  $\kappa = 1$ ,  $\sigma_1 = \rho$  and  $\alpha_1 = 1200$ . The densities along the line connecting  $(2, 0)$  and  $(7, 3)$  at  $t = 3.5$  and 5 are shown in Figure 5.11. One can see that MM-WENOMR with  $350 \times 150$  cells outperforms UM-WENOMR with  $1050 \times 450$  cells and MM-WENOJS with  $350 \times 150$  cells, and the small scale structures and the Kelvin-Helmholtz instability can be clearly observed by using MM-WENOMR. The CPU times in Table 5.2 show that MM-WENOMR with  $350 \times 150$  cells only takes 18.9% CPU time of MM-WENOMR with  $1050 \times 450$  cells and 9.8% CPU time more than MM-WENOJS with  $350 \times 150$  cells.

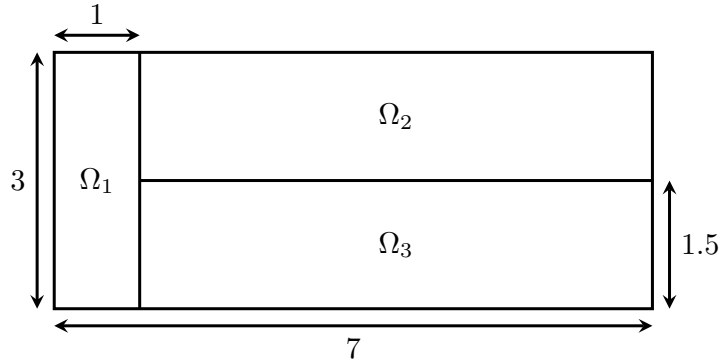


Figure 5.8: Example 5.7. Initial decomposition of  $\Omega_p$ .

**Example 5.8** (2D shock-bubble interaction I). This test is about the interaction of a shock wave with a helium cylindrical bubble [24], and has been frequently applied to numerical computations [39]. Initially, the domain  $\Omega_p = [0, 445] \times [-44.5, 44.5]$  is decomposed into three sub-domain as illustrated in Figure 5.12, and a Mach  $M_s = 1.22$  shock wave, positioned at  $x_1 = 275$ , moves through the quiescent air and will eventually meet a cylindrical helium bubble, centered at  $(x_1, x_2) = [225, 0]$  of radius 25, filled with the helium contaminated with 28% of air. Reflecting boundary conditions are specified on the top and bottom boundaries, while outflow and inflow boundary conditions are



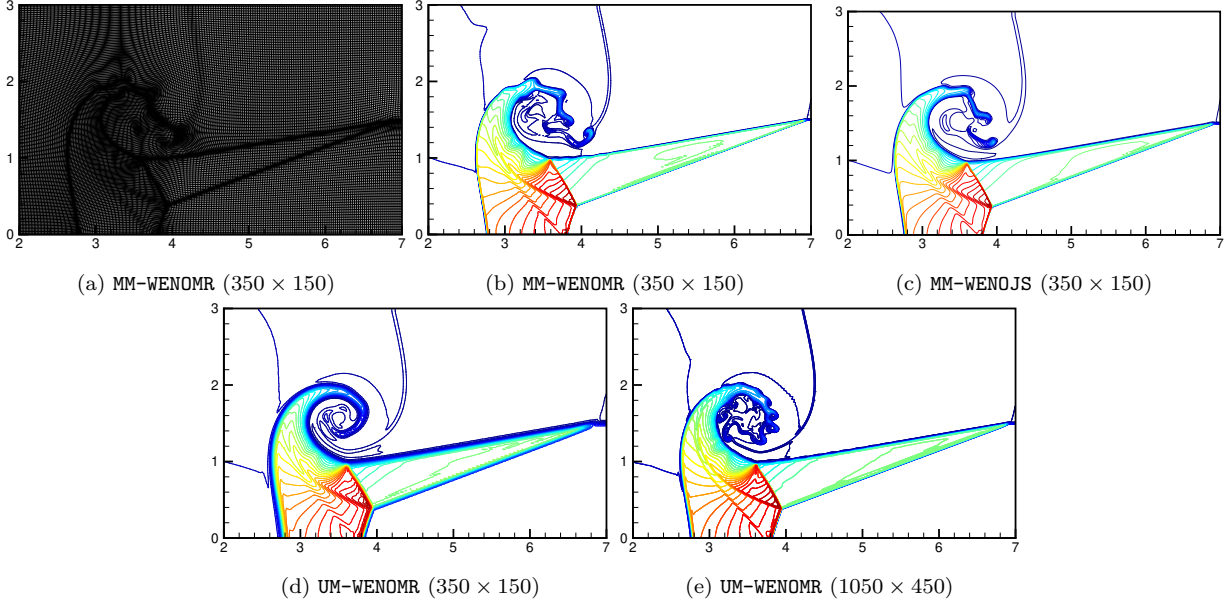


Figure 5.9: Example 5.7. Adaptive mesh of MM-WENOMR with  $350 \times 150$  cells and density contours (40 equally spaced contour lines) at  $t = 3.5$ .

applied on the left and right boundaries. The density of the bubble is determined based on the assumption that the regions  $\Omega_1$  and  $\Omega_2$  are in pressure and temperature equilibrium. Specially, the initial data are

$$(\rho_1, \rho_2, v_1, v_2, p) = \begin{cases} (\epsilon, 1.225 (R_1/R_2) - \epsilon, 0, 0, 101325), & (x_1, x_2) \in \Omega_1, \\ (1.225 - \epsilon, \epsilon, 0, 0, 101325), & (x_1, x_2) \in \Omega_2, \\ (1.6861 - \epsilon, \epsilon, -113.5243, 0, 159060), & (x_1, x_2) \in \Omega_3, \end{cases}$$

with  $\epsilon = 0.03$ ,  $\Gamma_1 = 1.4$ ,  $\Gamma_2 = 1.647$ ,  $p_{\infty,1} = p_{\infty,2} = 0$ ,  $R_1 = 0.287$ , and  $R_2 = 1.578$ .

Figures 5.13-5.14 show the adaptive meshes and the schlieren images by the function

$$\Phi = \exp(-\Psi|\nabla\rho|/|\nabla\rho|_{\max}), \quad (5.2)$$

with  $\Psi = (30\rho_1 + 150\rho_2) / \rho$  obtained by MM-WENOMR and UM-WENOMR at  $t = 0.02, 0.052, 0.076, 0.26, 0.452$ , and  $t = 0.676$  (after the bubble is first hit by the incident shock wave), where the monitor function is chosen as (4.2) with  $\kappa = 1$ ,  $\sigma_1 = \rho$  and  $\alpha_1 = 1000$ . Notice that the top and bottom half parts of the schlieren image are the results obtained respectively by MM-WENOMR and UM-WENOMR, and the velocity of the shock wave is  $-415.16$ , thus it takes about  $t = 0.06$  for the shock wave to meet the bubble. We see that the mesh points adaptively concentrate near the large gradient area

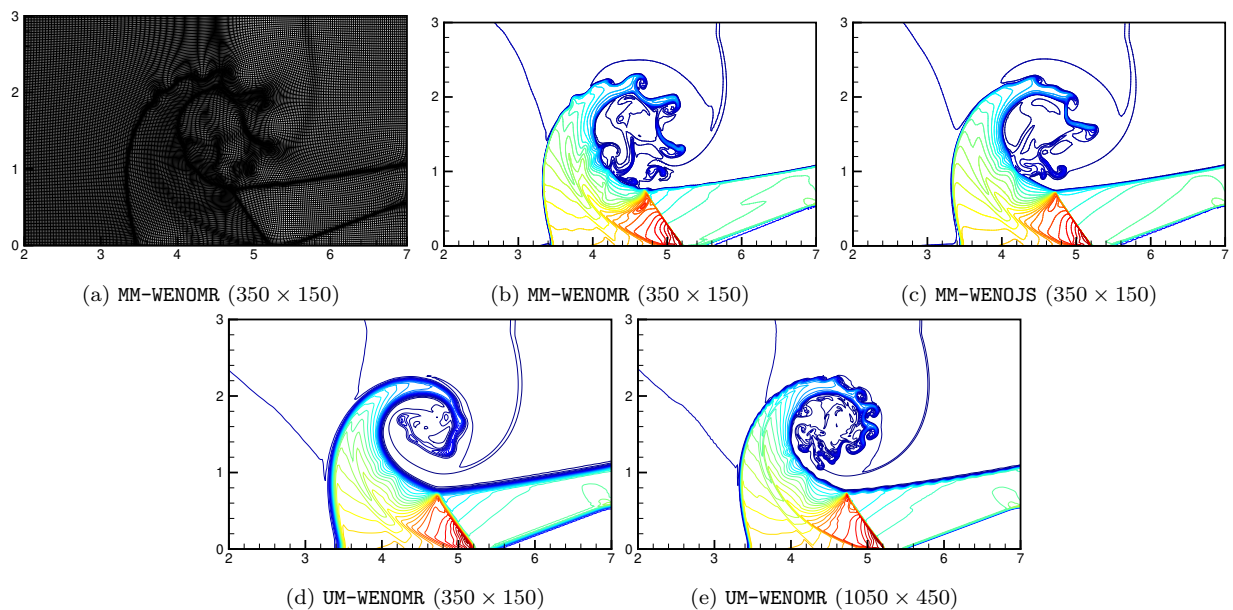


Figure 5.10: Same as Figure 5.9, except for  $t = 5$ .

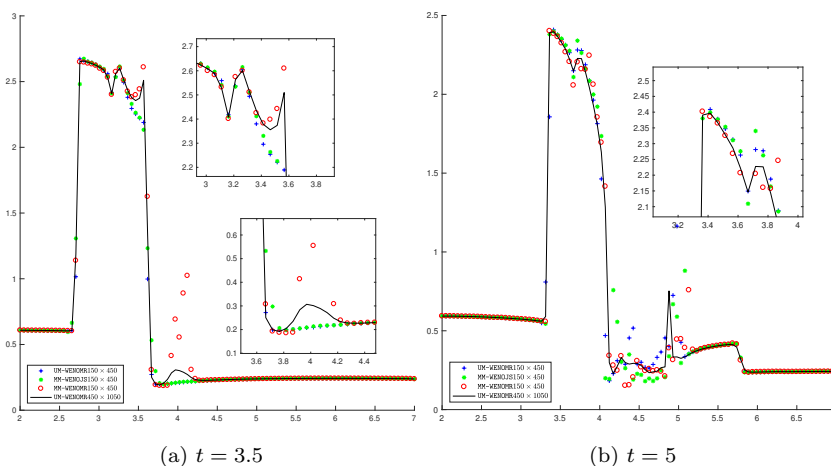


Figure 5.11: Example 5.7. Densities  $\rho$  along the line connecting  $(2, 0)$  and  $(7, 3)$  at  $t = 3.5$  and  $5$ , respectively.

of the density and MM-WENOMR captures the sharp bubble interfaces and some small wave structures well. Table 5.3 tells us that MM-WENOMR costs 26.2% CPU time of UM-WENOMR with a finer mesh, when it obtains even better results.

**Example 5.9 (2D shock-bubble interaction II).** The shock-bubble interaction problem is extended to the stiffened gas. The domain and the boundary conditions are the same as those in Example 5.8. Initially, the regions  $\Omega_2$  and  $\Omega_3$  are filled with the stiffened gas, while  $\Omega_1$  is filled with the

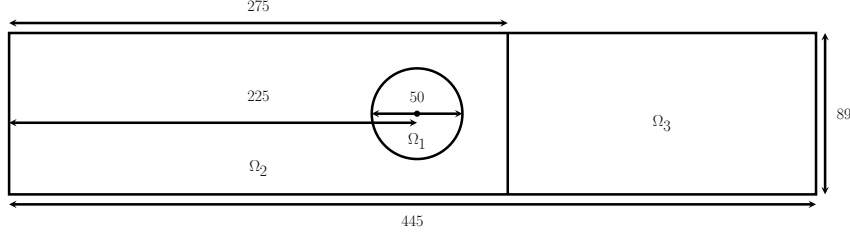


Figure 5.12: Example 5.8. Initial decomposition of  $\Omega_p$ .

	MM-WENOMR	UM-WENOMR	UM-WENOMR
Example 5.8	1h4m ( $800 \times 160$ cells)	9m12s ( $800 \times 160$ cells)	4h4m ( $2400 \times 480$ cells)
Example 5.9	9m28s ( $800 \times 160$ cells)	1m47s ( $800 \times 160$ cells)	40m11s ( $2400 \times 480$ cells)
Example 5.10	11h6m ( $400 \times 80 \times 80$ cells)	2h34m ( $400 \times 80 \times 80$ cells)	38h2m ( $800 \times 160 \times 160$ cells)
Example 5.11	2h9m ( $400 \times 80 \times 80$ cells)	46m32s ( $400 \times 80 \times 80$ cells)	11h58m ( $800 \times 160 \times 160$ cells)

Table 5.3: CPU times of Examples 5.8-5.11 (32 cores).

ideal gas, and a Mach  $M_s = 10$  shock wave at  $x_1 = 275$  moves to a cylindrical bubble centered at  $(x_1, x_2) = [225, 0]$ . Specially, the initial data are

$$(\rho_1, \rho_2, v_1, v_2, p) = \begin{cases} (\epsilon, 5 - \epsilon, 0, 0, 100), & (x_1, x_2) \in \Omega_1, \\ (1 - \epsilon, \epsilon, 0, 0, 100), & (x_1, x_2) \in \Omega_2, \\ (1.980198 - \epsilon, \epsilon, -121.2497, 0, 29800), & (x_1, x_2) \in \Omega_3, \end{cases}$$

with  $\epsilon = 0.05, \Gamma_1 = 3.0, p_{\infty,1} = 100, \Gamma_2 = 1.4, p_{\infty,2} = 0, c_{v,1} = c_{v,2} = 1$ .

Figure 5.15 presents the adaptive mesh obtained by MM-WENOMR with  $800 \times 160$  cells at  $t = 0.8$ , and Figure 5.16 gives the schlieren images at  $t = 0.8$ , where the monitor function is chosen as (4.2) with  $\kappa = 5$ ,  $(\sigma_1, \sigma_2, \sigma_3, \sigma_4, \sigma_5) = (\Phi, u, \rho_1, \rho_2, p)$ ,  $(\alpha_1, \alpha_2, \alpha_3, \alpha_4, \alpha_5) = (600, 500, 1200, 1200, 1200)$ , and the schlieren function is given by (5.2) with  $\Psi = (120\rho_1 + 20\rho_2) / \rho$ . We see that the mesh points adaptively concentrate near the shock wave and the bubble interfaces, MM-WENOMR with  $800 \times 160$  cells is better than UM-WENOMR with the same number of cells, MM-WENOMR can detect the sharp bubble interfaces well, and MM-WENOMR is efficient since the CPU time of MM-WENOMR with  $800 \times 160$  cells is 23.6% of UM-WENOMR with  $2400 \times 480$  cells shown in Table 5.3.

**Example 5.10** (3D shock-bubble interaction I). This is an extension of Example 5.8, and considers a planer shock wave interacting with a helium bubble in the domain  $[0, 445] \times [-44.5, 44.5] \times [-44.5, 44.5]$ . The initial pre- and post-shock states are

$$(\rho_1, \rho_2, v_1, v_2, v_3, p) = \begin{cases} (1.225 - \epsilon, \epsilon, 0, 0, 0, 101325), & x_1 < 275, \\ (1.6861 - \epsilon, \epsilon, -113.5243, 0, 0, 159060), & x_1 > 275, \end{cases}$$

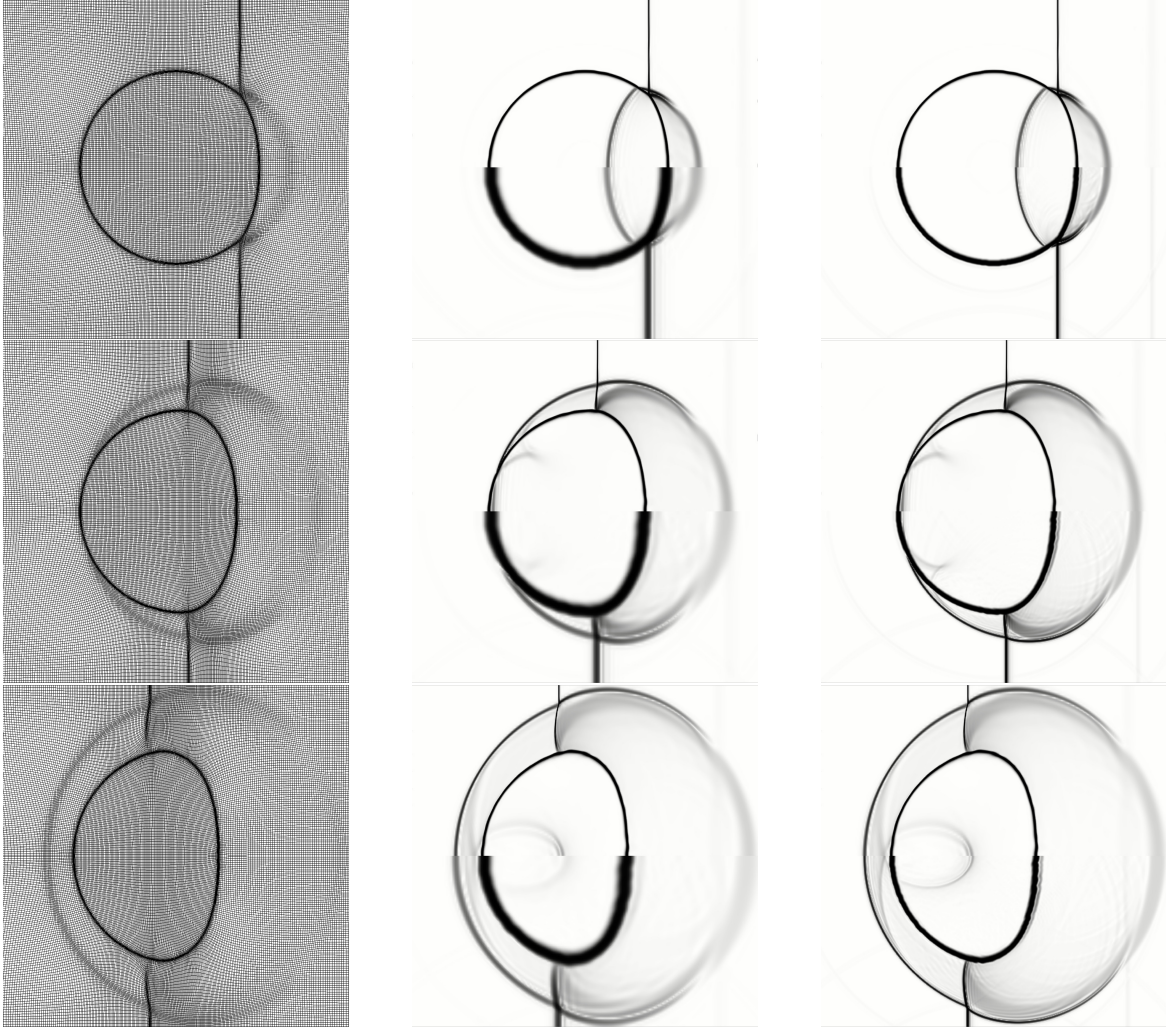


Figure 5.13: Example 5.8. From left to right: adaptive meshes of  $800 \times 160$  cells, schlieren images obtained by MM-WENOMR with  $800 \times 160$  cells (top half) and UM-WENOMR with  $800 \times 160$  cells (bottom half), and schlieren images by MM-WENOMR with  $800 \times 160$  cells (top half) and UM-WENOMR with  $2400 \times 480$  cells (bottom half). From top to bottom:  $t = 0.02, 0.052, 0.076$ .

and the bubble state is

$$(\rho_1, \rho_2, v_1, v_2, v_3, p) = (\epsilon, 1.225 (R_1/R_2) - \epsilon, 0, 0, 0, 101325), \quad \sqrt{(x_1 - 225)^2 + x_2^2 + x_3^2} < 25,$$

with  $\epsilon = 0.03, p_{\infty,1} = p_{\infty,2} = 0, \Gamma_1 = 1.4, \Gamma_2 = 1.647, R_1 = 0.287, R_2 = 1.578$ .

Figure 5.17 gives the close-up of the adaptive mesh, the iso-surface of  $\rho = 0.66$ , three offset 2D slices and two surface meshes near the bubble at  $t = 0.72$ , where the monitor function is chosen as (4.2) with  $\kappa = 1, \sigma_1 = \rho$  and  $\alpha_1 = 1200$ , and the linear weights of the multi-resolution WENO reconstruction are taken as  $\chi_1 = 0.95, \chi_2 = 0.045$  and  $\chi_3 = 0.005$ . Figure 5.18 shows the schlieren images on the slice  $x_3 = 0$  given by (5.2) with  $\Psi = (10\rho_1 + 30\rho_2)/\rho$ , where the top half parts

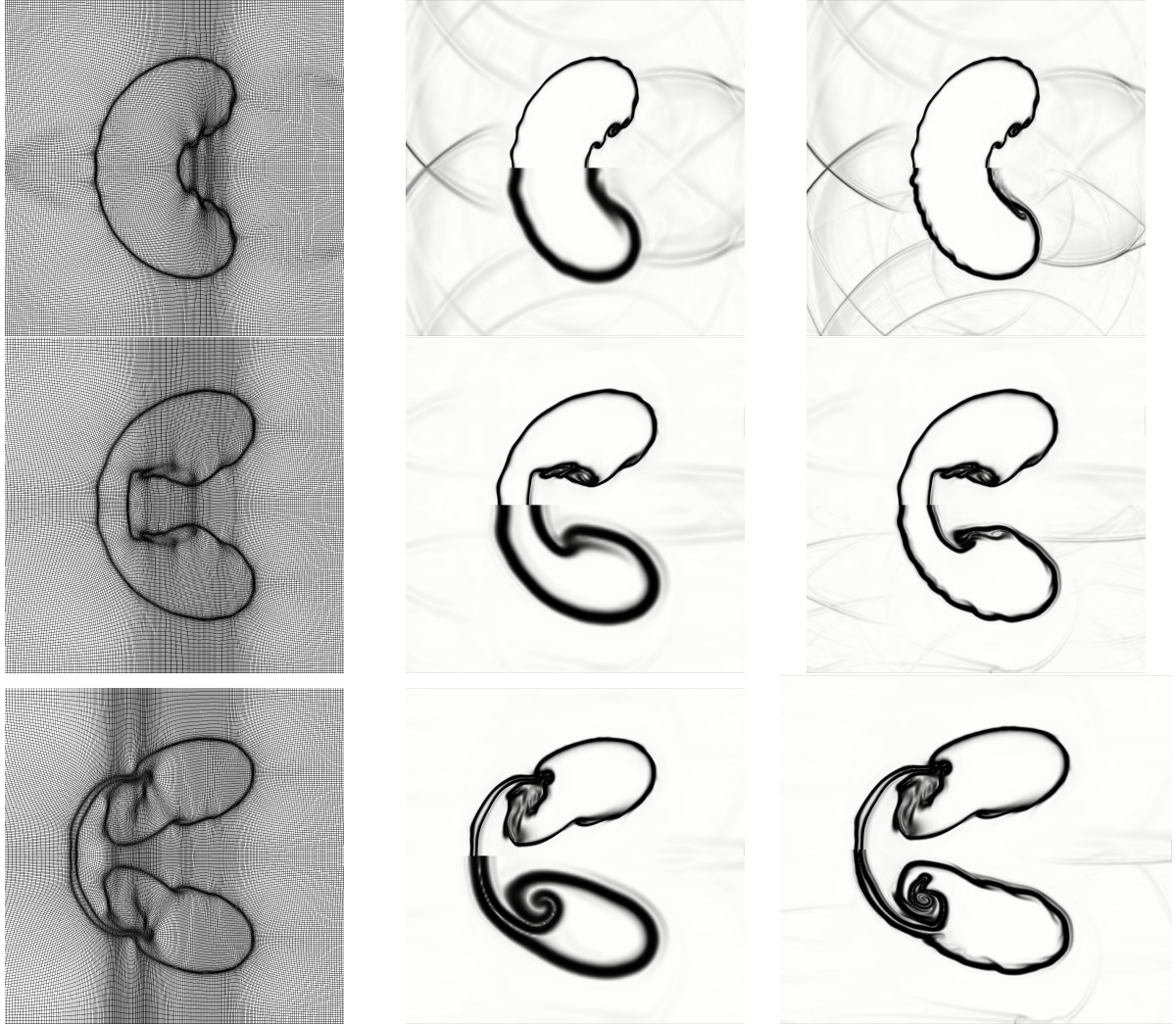


Figure 5.14: Same as Figure 5.13 except for  $t = 0.26, 0.452, 0.676$ .

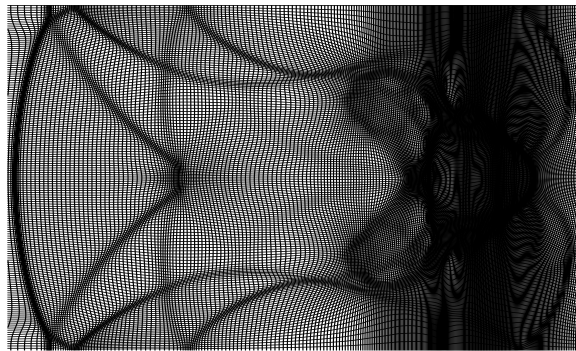


Figure 5.15: Example 5.9. Adaptive mesh obtained by MM-WENOMR with  $800 \times 160$  cells at  $t = 0.8$ .

are the results obtained by MM-WENOMR with  $400 \times 80 \times 80$  cells, while the left and right bottom half parts are those obtained by UM-WENOMR with  $400 \times 80 \times 80$  cells and  $800 \times 160 \times 160$  cells,

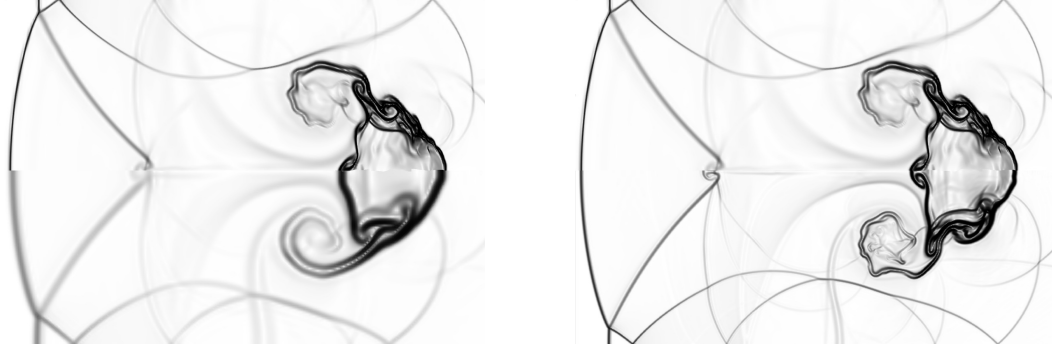


Figure 5.16: Example 5.9. Schlieren images of  $\Phi$  at  $t = 0.8$ . Left: MM-WENO with  $800 \times 160$  cells (top half) and UM-WENO with  $800 \times 160$  cells (bottom half); right: MM-WENO with  $800 \times 160$  cells (top half) and UM-WENO with  $2400 \times 480$  cells (bottom half).

respectively. One can see that the solution of MM-WENO with  $400 \times 80 \times 80$  cells is comparable to that of UM-WENO with  $800 \times 160 \times 160$  cells, but the CPU time of MM-WENO with  $400 \times 80 \times 80$  cells is 29.2% of UM-WENO with  $800 \times 160 \times 160$  cells, see Table 5.3.

**Example 5.11** (3D shock-bubble interaction II). This test considers an extended 3D problem of the interaction of the shock wave and the bubble in the domain  $[0, 445] \times [-44.5, 44.5] \times [-44.5, 44.5]$ . A bubble of ideal gas initially located at  $(x_1, x_2, x_3) = [225, 0, 0]$  with radius  $r = 25$  is surrounded by a stiffened gas. The initial pre- and post-shock states are

$$(\rho_1, \rho_2, v_1, v_2, v_3, p) = \begin{cases} (1 - \epsilon, \epsilon, 0, 0, 0, 100), & x_1 < 275, \\ (1.980198 - \epsilon, \epsilon, -121.2497, 0, 0, 29800), & x_1 > 275, \end{cases}$$

and the bubble state is

$$(\rho_1, \rho_2, v_1, v_2, v_3, p) = (\epsilon, 5 - \epsilon, 0, 0, 0, 100), \quad \sqrt{(x_1 - 225)^2 + x_2^2 + x_3^2} < 25,$$

where  $\epsilon = 0.05$ ,  $c_{v,1} = c_{v,2} = 1$ ,  $\Gamma_1 = 3.0$ ,  $p_{\infty,1} = 100$ ,  $\Gamma_2 = 1.4$ ,  $p_{\infty,2} = 0$ .

Figure 5.19 shows the close-up of the adaptive mesh, the iso-surfaces of  $\rho = 11.11$ , three offset 2D slices and two surface meshes near the bubble at  $t = 0.64$ , and Figure 5.20 gives the schlieren images given by the function in (5.2) with  $\Psi = (20\rho_1 + 5\rho_2) / \rho$  at different times, where the monitor function is chosen as (4.2) with  $(\sigma_1, \sigma_2) = (\rho_1, p)$  and  $(\alpha_1, \alpha_2) = (500, 500)$ , and the linear weights of the multi-resolution WENO reconstruction are the same as those in Example 5.10. It is shown that the solution given by MM-WENO is superior to the solution given by UM-WENO with finer mesh, while MM-WENO is efficient since the CPU time of MM-WENO with  $400 \times 80 \times 80$  cells is 18.0% of UM-WENO with  $800 \times 160 \times 160$  cells, see Table 5.3.

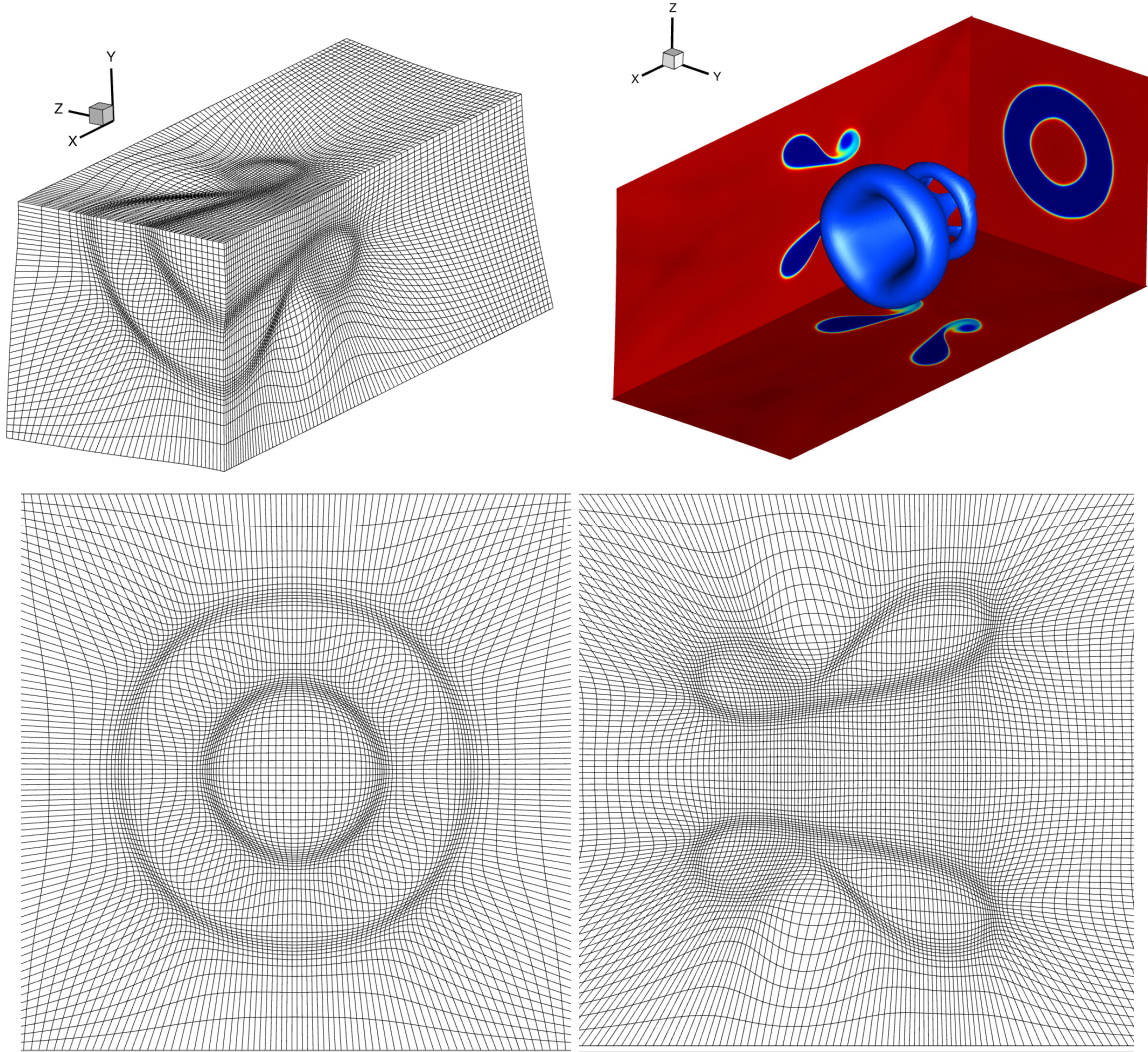


Figure 5.17: Example 5.10. Adaptive meshes and  $\rho$  at  $t = 0.72$ . Top left: close-up of the adaptive mesh,  $i_1 \in [40, 130]$ ,  $i_2 \in [1, 40]$ ,  $i_3 \in [40, 80]$ ; top right: the iso-surface of  $\rho = 0.66$  and three offset 2D slices taken at  $x_1 = 136$ ,  $x_2 = 0$ ,  $x_3 = 0$ ; bottom left: the surface mesh with  $i_1 = 120$ ; bottom right: the surface mesh with  $i_3 = 40$ .

## 6. Conclusion

This paper extended the high-order entropy stable (ES) adaptive moving mesh finite difference schemes developed in [14] to the two- and three-dimensional (multi-component) compressible Euler equations with the stiffened equation of state. The two-point entropy conservative (EC) flux in the curvilinear coordinates was first constructed according to the sufficient condition, and then combined with the high-order discretization of the GCLs to derive the high-order semi-discrete EC schemes. To ensure the entropy stability and to suppress the numerical oscillation, the high-order ES schemes were constructed by adding some suitable high-order dissipation terms based on the multi-

resolution WENO reconstruction for the scaled entropy variables to the high-order EC schemes. The high-order explicit strong-stability-preserving Runge-Kutta time discretization was implemented to obtain the fully-discrete high-order schemes, which could preserve the free-stream states and where the mesh points were adaptively redistributed by solving the mesh iterative redistribution equations with an appropriately chosen monitor function. Several 2D and 3D numerical tests were conducted on the parallel computer system with the MPI programming to validate the accuracy and the ability to resolve effectively the localized structures of the present schemes.

## Acknowledgments

The authors were partially supported by the National Numerical Windtunnel project, the National Key R&D Program of China (Project Number 2020YFA0712000), the National Natural Science Foundation of China (No. 12126302 & 12171227), and High-performance Computing Platform of Peking University.

## Appendix A. Multi-resolution WENO reconstruction

This appendix outlines the 1D fifth-order multi-resolution WENO reconstruction proposed in [49]. Different from the classical WENO reconstruction [28], it uses three unequal-sized central stencils to get the WENO reconstructed polynomial with any positive linear weights whose sum is one, and can achieve the expected accuracy in the smooth regions and the good performance in capturing sharp shock transitions. For the given cell average values  $\{W_j\}$ , the fifth-order reconstruction process for  $W_{j\pm\frac{1}{2}}^{\text{WENO}}$  is described as follows.

1. For each  $j$ , select three central spatial stencils  $[\xi_{j-m+\frac{1}{2}}, \xi_{j+m-\frac{1}{2}}]$ ,  $m = 1, 2, 3$ , and then reconstruct  $(2m - 2)$ th degree polynomials  $h_m(\xi)$ ,  $m = 1, 2, 3$ , respectively, by

$$\begin{aligned} \frac{1}{\Delta\xi} \int_{\xi_{l-\frac{1}{2}}}^{\xi_{l+\frac{1}{2}}} h_1(\xi) d\xi &= W_l, \quad l = j, \\ \frac{1}{\Delta\xi} \int_{\xi_{l-\frac{1}{2}}}^{\xi_{l+\frac{1}{2}}} h_2(\xi) d\xi &= W_l, \quad l = j - 1, j, j + 1, \\ \frac{1}{\Delta\xi} \int_{\xi_{l-\frac{1}{2}}}^{\xi_{l+\frac{1}{2}}} h_3(\xi) d\xi &= W_l, \quad l = j - 2, j - 1, j, j + 1, j + 2. \end{aligned}$$

Those polynomials  $\{h_m(\xi)\}$  can be explicitly given by

$$\begin{aligned} h_1(\xi) &= W_j, \quad h_2(\xi) = a_1 L_1(\xi) + a_2 L_2(\xi) + a_3 L_3(\xi), \\ h_3(\xi) &= b_1 L_1(\xi) + b_2 L_2(\xi) + b_3 L_3(\xi) + b_4 L_4(\xi) + b_5 L_5(\xi), \end{aligned} \tag{A.1}$$



where  $L_\ell$ ,  $\ell = 1, \dots, 5$ , are the (local) Legendre basis functions

$$\begin{aligned} L_1(\xi) &= 1, & L_2(\xi) &= \frac{\xi - \xi_j}{\Delta\xi}, & L_3(\xi) &= \left(\frac{\xi - \xi_j}{\Delta\xi}\right)^2 - \frac{1}{12}, \\ L_4(\xi) &= \left(\frac{\xi - \xi_j}{\Delta\xi}\right)^3 - \frac{3}{20} \left(\frac{\xi - \xi_j}{\Delta\xi}\right), & L_5(\xi) &= \left(\frac{\xi - \xi_j}{\Delta\xi}\right)^4 - \frac{3}{14} \left(\frac{\xi - \xi_j}{\Delta\xi}\right)^2 + \frac{3}{560}, \end{aligned}$$

and the coefficients  $a_m, b_\ell$ ,  $m = 1, \dots, 3, \ell = 1, \dots, 5$ , are calculated by

$$\begin{aligned} a_1 &= W_j, & a_2 &= \frac{W_{j+1} - W_{j-1}}{2}, & a_3 &= \frac{W_{j-1} - 2W_j + W_{j+1}}{2}, \\ b_1 &= W_j, & b_2 &= \frac{11W_{j-2} - 82W_{j-1} + 82W_{j+1} - 11W_{j+2}}{120}, \\ b_3 &= \frac{-3W_{j-2} + 40W_{j-1} - 74W_j + 40W_{j+1} - 3W_{j+2}}{56}, \\ b_4 &= \frac{-W_{j-2} + 2W_{j-1} - 2W_{j+1} + W_{j+2}}{12}, \\ b_5 &= \frac{W_{j-2} - 4W_{j-1} + 6W_j - 4W_{j+1} + W_{j+2}}{24}. \end{aligned}$$

2. Compute the smoothness indicators  $\beta_m$ ,  $m = 1, 2, 3$ , by

$$\beta_1 = \min \left( (W_j - W_{j-1})^2, (W_{j+1} - W_j)^2 \right),$$

and

$$\beta_m = \sum_{\alpha=1}^{2m-2} \int_{\xi_{j-m+\frac{1}{2}}}^{\xi_{j+m-\frac{1}{2}}} (\Delta\xi)^{2\alpha-1} \left( \frac{d^\alpha h_m(\xi)}{d\xi^\alpha} \right)^2 d\xi, \quad m = 2, 3. \quad (\text{A.2})$$

Substituting (A.1) into (A.2) gives

$$\beta_2 = a_2^2 + \frac{13}{3}a_3^2, \quad \beta_3 = \left( b_2 + \frac{1}{10}b_4 \right)^2 + \frac{13}{3} \left( b_3 + \frac{123}{455}b_5 \right)^2 + \frac{781}{20}b_4^2 + \frac{1421461}{2275}b_5^2.$$

The above  $\beta_1$  avoids the zero value of  $\beta_1$  calculated by (A.2) and the zeroth degree polynomial  $h_1(\xi)$ .

3. Choose the linear weights  $\chi_1 = 1/111, \chi_2 = 10/111, \chi_3 = 100/111$ , unless otherwise stated, and compute the nonlinear weights  $\{\hat{\omega}_m\}$  by

$$\hat{\omega}_m = \frac{\bar{\omega}_m}{\sum_{\ell=1}^3 \bar{\omega}_\ell}, \quad m = 1, 2, 3,$$

with

$$\bar{\omega}_m = \chi_m \left( 1 + \frac{\tau}{\varepsilon + \beta_m} \right), \quad \tau = \left( \frac{|\beta_3 - \beta_1| + |\beta_3 - \beta_2|}{2} \right)^2,$$

where  $\varepsilon$  is taken as  $10^{-10}$  to avoid the denominator becoming zero. In practice, the linear weights can be any positive numbers whose sum is one. If the linear weight corresponding to the five-point sub-stencil takes a relatively large value, then sharper transitions in discontinuous regions can be obtained, but the numerical solution may tend to oscillate.

4. The reconstructed value  $W_{j+\frac{1}{2}}^{\text{WENO}}$  by the fifth-order multi-resolution WENO reconstruction is computed by

$$W_{j+\frac{1}{2}}^{\text{WENO}} = \hat{\omega}_1 h_1 \left( x_{j+\frac{1}{2}} \right) + \hat{\omega}_2 h_2 \left( x_{j+\frac{1}{2}} \right) + \hat{\omega}_3 \left[ \frac{1}{\chi_3} h_3 \left( x_{j+\frac{1}{2}} \right) - \sum_{m=1}^2 \frac{\chi_m}{\chi_3} h_m \left( x_{j+\frac{1}{2}} \right) \right],$$

while  $W_{j-\frac{1}{2}}^{\text{WENO}}$  may be obtained by using the mirror-symmetry with respect to  $x_j$ .

## References

- [1] D. Bhowmik and H. Kumar, Entropy-stable schemes for relativistic hydrodynamics equations, *Z. Angew. Math. Phys.*, 71 (2020), 1–29.
- [2] B. Biswas and R.K. Dubey, Low dissipative entropy stable schemes using third order WENO and TVD reconstructions, *Adv. Comput. Math.*, 44 (2018), 1153–1181.
- [3] W. Boscheri and M. Dumbser, A direct Arbitrary-Lagrangian–Eulerian ADER-WENO finite volume scheme on unstructured tetrahedral meshes for conservative and non-conservative hyperbolic systems in 3D, *J. Comput. Phys.*, 275 (2014), 484–523.
- [4] J.U. Brackbill, An adaptive grid with directional control, *J. Comput. Phys.*, 108 (1993), 38–50.
- [5] J.U. Brackbill and J.S. Saltzman, Adaptive zoning for singular problems in two dimensions, *J. Comput. Phys.*, 46 (1982), 342–368.
- [6] M. Brio, A. Zakharian, and G. Webb, Two-dimensional Riemann solver for Euler equations of gas dynamics, *J. Comput. Phys.*, 167 (2001), 177–195.
- [7] C.J. Budd, W.Z. Huang, and R.D. Russell, Adaptivity with moving grids, *Acta Numer.*, 18 (2009), 111–241.
- [8] W.M. Cao, W.Z. Huang, and R.D. Russell, An r-adaptive finite element method based upon moving mesh PDEs, *J. Comput. Phys.*, 149 (1999), 221–244.
- [9] M.H. Carpenter, T.C. Fisher, E.J. Nielsen, and S.H. Frankel, Entropy stable spectral collocation schemes for the Navier-Stokes equations: Discontinuous interfaces, *SIAM J. Sci. Comput.*, 36 (2014), B835–B867.
- [10] H.D. Ceniceros and T.Y. Hou, An efficient dynamically adaptive mesh for potentially singular solutions, *J. Comput. Phys.*, 172 (2001), 609–639.

- [11] T.H. Chen and C.-W. Shu, Review of entropy stable discontinuous Galerkin methods for systems of conservation laws on unstructured simplex meshes, *CSIAM Trans. Appl. Math.*, 1 (2020), 1–52.
- [12] S.F. Davis, An interface tracking method for hyperbolic systems of conservation laws, *Appl. Numer. Math.*, 10 (1992), 447–472.
- [13] S.F. Davis and J.E. Flaherty, An adaptive finite element method for initial-boundary value problems for partial differential equations, *SIAM J. Sci. Stat. Comput.*, 3 (1982), 6–27.
- [14] J.M. Duan and H.Z. Tang, High-order accurate entropy stable adaptive moving mesh finite difference schemes for special relativistic (magneto)hydrodynamics, *J. Comput. Phys.*, online (2022), 111038.
- [15] J.M. Duan and H.Z. Tang, High-order accurate entropy stable finite difference schemes for one- and two-dimensional special relativistic hydrodynamics, *Adv. Appl. Math. Mech.*, 12 (2020), 1–29.
- [16] J.M. Duan and H.Z. Tang, High-order accurate entropy stable nodal discontinuous Galerkin schemes for the ideal special relativistic magnetohydrodynamics, *J. Comput. Phys.*, 421 (2020), 109731.
- [17] J.M. Duan and H.Z. Tang, Entropy stable adaptive moving mesh schemes for 2D and 3D special relativistic hydrodynamics, *J. Comput. Phys.*, 426 (2021), 109949.
- [18] G. Fernandez and B. Larrouturou, Hyperbolic schemes for multi-component Euler equations, in *Nonlinear Hyperbolic Equations-Theory, Computation Methods, and Applications (Aachen, 1988)*, vol. 24 of *Notes Numer. Fluid Mech.* (1989), 128–138.
- [19] U.S. Fjordholm, S. Mishra, and E. Tadmor, Arbitrarily high-order accurate entropy stable essentially non-oscillatory schemes for systems of conservation laws, *SIAM J. Numer. Anal.*, 50 (2012), 544–573.
- [20] S. Galera, P.H. Maire, and J. Breil, A two-dimensional unstructured cell-centered multi-material ALE scheme using VOF interface reconstruction, *J. Comput. Phys.*, 229 (2010), 5755–5787.
- [21] G.J. Gassner, A skew-symmetric discontinuous Galerkin spectral element discretization and its relation to SBP-SAT finite difference methods, *SIAM J. Sci. Comput.*, 35 (2013), 1233–1253.

- [22] S. Gottlieb, C.-W. Shu, and E. Tadmor, Strong stability-preserving high-order time discretization methods, *SIAM Rev.*, 43 (2001), 89–112.
- [23] A. Gouasmi, K. Duraisamy, and S.M. Murman, Formulation of entropy-stable schemes for the multicomponent compressible Euler equations, *Comput. Methods Appl. Mech. Engrg.*, 363 (2020), 112912.
- [24] J. Haas and B. Sturtevant, Interaction of weak shock waves with cylindrical and spherical gas inhomogeneities, *J. Fluid Mech.*, 181 (1987), 41–76.
- [25] A. Habbal, A. Dervieux, H. Guillard, and B. Larrouturou, Explicit calculation of reactive flows with an upwind finite element hydrodynamical code, *INRIA*, (1987).
- [26] A. Hildebrand and S. Mishra, Entropy stable shock capturing space-time discontinuous Galerkin schemes for systems of conservation laws, *Numer. Math.*, 126 (2014), 103–151.
- [27] F. Ismail and P.L. Roe, Affordable, entropy-consistent Euler flux functions II : Entropy production at shocks, *J. Comput. Phys.*, 228 (2009), 5410–5436.
- [28] G.S. Jiang and C.-W. Shu, Efficient implementation of weighted WENO schemes, *J. Comput. Phys.*, 126 (1996), 202–228.
- [29] B. Larrouturou, How to preserve the mass fractions positivity when computing compressible multi-component flows, *J. Comput. Phys.*, 95 (1991), 59–84.
- [30] B. Larrouturou and L. Fezoui, On the equations of multi-component perfect of real gas inviscid flow, In *Nonlinear Hyperbolic Problems* (edited by C. Carasso, P. Charrier, B. Hanouzet, and J.L. Joly), Lecture Notes in Mathematics, vol 1402, Springer, Berlin, Heidelberg, 1989, 69-98.
- [31] P.D. Lax and X.D. Liu, Solution of two-dimensional Riemann problems of gas dynamics by positive schemes, *SIAM J. Sci. Comput.*, 19 (1998), 319–340.
- [32] O. Le Métayer, J. Massoni, and R. Saurel, Elaborating equations of state of a liquid and its vapor for two-phase flow models, *Int. J. Thermal Sciences*, 43 (2004), 265–276.
- [33] P.G. LeFloch, J.M. Mercier, and C. Rohde, Fully discrete entropy conservative schemes of arbitrary order, *SIAM J. Numer. Anal.*, 40 (2002), 1968–1992.
- [34] A. Mignone, G. Bodo, S. Massaglia, T. Matsakos, O. Tesileanu, C. Zanni, and A. Ferrari, PLUTO: A numerical code for computational astrophysics, *Astrophys. J. Suppl. Ser.*, 170 (2007), 228–242.

- [35] G.H. Miller and E.G. Puckett, A high-order godunov method for multiple condensed phases, *J. Comput.Phys.*, 128 (1996), 134–164.
- [36] K. Miller, Moving finite elements. II, *SIAM J. Numer. Anal.*, 18 (1981), 1033–1057.
- [37] W. Mulder, S. Osher, and J.A. Sethian, Computing interface motion in compressible gas dynamics, *J. Comput. Phys.*, 100 (1992), 209–228.
- [38] E. Puckett and J. Saltzman, A 3D adaptive mesh refinement algorithm for multimaterial gas dynamics, *Phys. D*, 60 (1992), 84–93.
- [39] J.J. Quirk and S. Karni, On the dynamics of a shock–bubble interaction, *J. Fluid Mech.*, 318 (1996), 129–163.
- [40] W.Q. Ren and X.P. Wang, An iterative grid redistribution method for singular problems in multiple dimensions, *J. Comput. Phys.*, 159 (2000), 246–273.
- [41] F. Renac, Entropy stable, robust and high-order DGSEM for the compressible multicomponent Euler equations, *J. Comput. Phys.*, 445 (2021), 110584.
- [42] K.M. Shyue, An efficient shock-capturing algorithm for compressible multicomponent problems, *J. Comput.Phys.*, 142 (1998), 208–242.
- [43] J.M. Stockie, J.A. Mackenzie, and R.D. Russell, A moving mesh method for one-dimensional hyperbolic conservation laws, *SIAM J. Sci. Comput.*, 22 (2001), 1791–1813.
- [44] E. Tadmor, The numerical viscosity of entropy stable schemes for systems of conservation laws, I, *Math. Comp.*, 49 (1987), 91–103.
- [45] E. Tadmor, Entropy stability theory for difference approximations of nonlinear conservation laws and related time-dependent problems, *Acta Numer.*, 12 (2003), 451–512.
- [46] T. Tang, Moving mesh methods for computational fluid dynamics, *Contemp. Math.*, 383 (2005), 141–173.
- [47] M.R. Visbal and D.V. Gaitonde, On the use of higher-order finite-difference schemes on curvilinear and deforming meshes, *J. Comput. Phys.*, 181 (2002), 155–185.
- [48] D.S. Wang and X.P. Wang, A three-dimensional adaptive method based on the iterative grid redistribution, *J. Comput. Phys.*, 199 (2004), 423–436.

- [49] Z. Wang, J. Zhu, L. Tian, Y. Yang, and N. Zhao, An efficient fifth-order finite difference multi-resolution WENO scheme for inviscid and viscous flow problems, *Comput. & Fluids*, 230 (2021), 105138.
- [50] A.M. Winslow, Numerical solution of the quasilinear Poisson equation in a nonuniform triangle mesh, *J. Comput. Phys.*, 1 (1967), 149–172.
- [51] H. Wu and Z.J. Shen, A general Riemann solver for Euler equations, *Int. J. Numer. Meth Fluids*, 56 (2008), 1993–2020.
- [52] K.L. Wu and C.-W. Shu, Entropy symmetrization and high-order accurate entropy stable numerical schemes for relativistic MHD equations, *SIAM J. Sci. Comput.*, 42 (2020), A2230–A2261.
- [53] K. Xu, BGK-based scheme for multicomponent flow calculations, *J. Comput. Phys.*, 134 (1997), 122–133.
- [54] H. Zhang, M. Reggio, J.Y. Trépanier, and R. Camarero, Discrete form of the GCL for moving meshes and its implementation in CFD schemes, *Comput. & Fluids*, 22 (1993), 9–23.



Figure 5.18: Example 5.10. Schlieren images  $\Phi$  on the slice  $x_3 = 0$  at  $t = 0.08, 0.24, 0.40, 0.56, 0.72$  (from top to bottom). Left: MM-WENOMR (top half) and UM-WENOMR (bottom half) with  $400 \times 80 \times 80$  cells; right: MM-WENOMR with  $400 \times 80 \times 80$  cells (top half) and UM-WENOMR with  $800 \times 160 \times 160$  cells (bottom half).

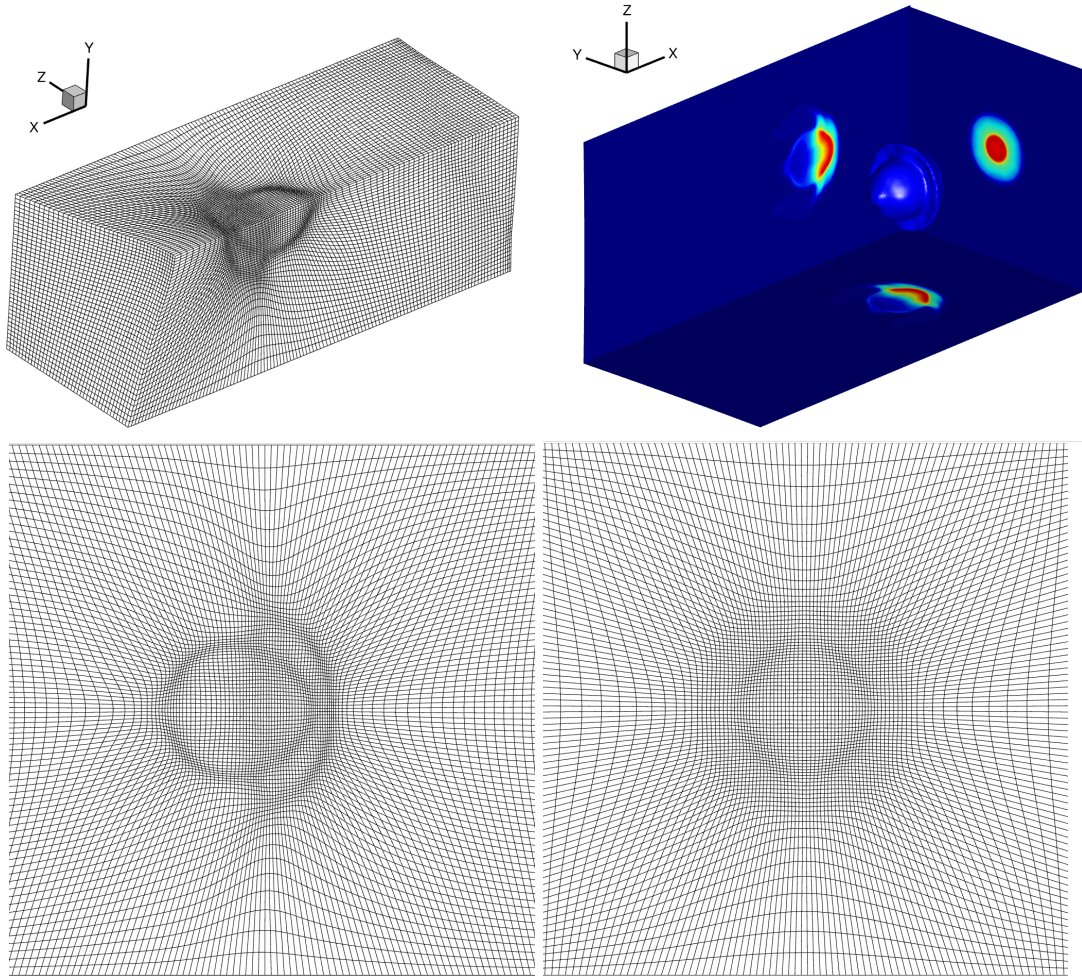


Figure 5.19: Example 5.11. Adaptive meshes and  $\rho$  at  $t = 0.64$ . Top left: close-up of the adaptive mesh,  $i_1 \in [100, 230]$ ,  $i_2 \in [1, 40]$ ,  $i_3 \in [40, 80]$ ; top right: the iso-surface of  $\rho = 11.11$  and three offset 2D slices taken at  $x_1 = 214$ ,  $x_2 = 0$ ,  $x_3 = 0$ ; bottom left: the surface mesh with  $i_1 = 180$ ; bottom right: the surface mesh with  $i_2 = 40$ .





Figure 5.20: Example 5.11. Schlieren images  $\Phi$  on  $x_3 = 0$  at  $t = 0.16, 0.32, 0.48, 0.64$  (from top to bottom). Left: MM-WENOMR (top half) and UM-WENOMR (bottom half) with  $400 \times 80 \times 80$  cells; right: MM-WENOMR with  $400 \times 80 \times 80$  cells (top half) and UM-WENOMR with  $800 \times 160 \times 160$  cells (bottom half).